Title

Structure of human telomerase holoenzyme with bound telomeric DNA

Journal

Nature, 593(7859)

ISSN

0028-0836

Authors

Ghanim, George E

Fountain, Adam J

van Roon, Anne-Marie M

et al.

Publication Date

2021-05-20

DOI

10.1038/s41586-021-03415-4

Peer reviewed

Published in final edited form as:
Nature. 2021 May 01; 593(7859): 449–453. doi:10.1038/s41586-021-03415-4.

Structure of human telomerase holoenzyme with bound telomeric DNA

George E. Ghanim[#1], **Adam J. Fountain**[#1], **Anne-Marie M van Roon**[#1], **Ramya Rangan**[2], **Rhiju Das**[3,4], **Kathleen Collins**[5,6], **Thi Hoang Duong Nguyen**[1]

[1]Medical Research Council Laboratory of Molecular Biology, Francis Crick Avenue, Cambridge, CB2 0QH, United Kingdom

[2]Biophysics Program, Stanford University, Stanford, California, 94305, USA

[3]Department of Biochemistry, Stanford University, Stanford, California 94305, USA

[4]Department of Physics, Stanford University, Stanford, California 94305, USA

[5]Department of Molecular and Cell Biology, University of California, Berkeley, California 94720, USA

[6]California Institute for Quantitative Biology (QB3), University of California, Berkeley, California 94720, USA

[#] These authors contributed equally to this work.

Abstract

Telomerase adds telomeric repeats at chromosome ends to compensate for telomere loss caused by incomplete genome end replication1. In humans, telomerase is upregulated during embryogenesis and in cancers, while mutations that compromise its function result in diseases2. Our previous 8 Å human telomerase structure revealed vertebrate-specific composition and architecture3, consisting of a catalytic core flexibly tethered to an H/ACA ribonucleoprotein (RNP) lobe by telomerase RNA. To effectively modulate telomerase activity as a therapeutic approach against cancers and diseases, high-resolution structural information is necessary. Here we present the structure of human telomerase holoenzyme bound to a telomeric DNA, determined by cryo-electron microscopy (cryo-EM) at 3.4 Å resolution for the H/ACA RNP and 3.8 Å resolution for the catalytic core. The structure reveals crucial DNA/RNA binding interfaces in telomerase active site

Correspondence to: Thi Hoang Duong Nguyen.

Correspondence and requests for materials should be addressed to T.H.D.N (knguyen@mrc-lmb.cam.ac.uk).

Author contributions

K.C. and T.H.D.N. initiated the project. T.H.D.N. collected and analyzed EM data. G.E.G., A.J.F., A.M.v.R. and T.H.D.N. performed manual model building and refinement and analyzed the structures. R. R. and R. D. performed all DRRAFTER modelling of RNA and ERRASER for improving RNA geometry. G.E.G., and A.M.v.R. and T.H.D.N. performed all biochemical experiments. G.E.G. and A.J.F performed all quantifications. T.H.D.N. wrote the paper with inputs from all authors.

Author information

Reprints and permissions information is available at www.nature.com/reprints. The authors declare no competing financial interests. Readers are welcome to comment on the online version of the paper. Cryo-EM maps of the catalytic core, H/ACA lobe and the two overall human telomerase holoenzyme classes will be deposited with the Electron Microscopy Database under accession number EMD-12174, EMD-12177, EMD-12175 and EMD-12176, respectively. PDB coordinates of the catalytic core and H/ACA RNP will be deposited with the Protein Data Bank under accession number PDB ID 7BG9 and PDB 7BGB, respectively.

Europe PMC Funders Author Manuscripts

and locations of mutations that alter telomerase activity. We identified a histone H2A-H2B dimer within the holoenzyme bound to an essential telomerase RNA motif, suggesting an unexpected role for histones in telomerase RNA folding and function. Furthermore, the first high-resolution structure of a eukaryotic H/ACA RNP reveals the molecular recognition of conserved RNA and protein motifs and new interactions crucial for understanding the molecular pathology of many disease mutations. Our findings illuminate unanticipated structural details of human telomerase assembly and active site, paving the way for the development of telomerase-targeting therapeutics.

Telomerase synthesizes telomeric repeats (TTAGGG in humans) at eukaryotic chromosome ends using an integral RNA template within telomerase RNA (TER or hTR in humans) and a telomerase reverse transcriptase subunit (TERT)[4]. As with other polymerases, telomerase synthesis of a single telomeric repeat involves repetitive cycles of nucleotide addition[5]. Additionally, telomerase has a unique ability to synthesize multiple telomeric repeats with each binding event, *i.e.* repeat addition processivity (RAP)[6]. Despite numerous structural characterizations, the structural determinants for human telomerase activity remain poorly understood due to the lack of high-resolution structure of human TERT. Vertebrate telomerase RNAs contain a 3' H/ACA domain essential for telomerase RNP biogenesis and regulation[3,7]. This H/ACA domain is shared with an evolutionarily conserved family of non-coding RNAs including the small nucleolar (sno) and small Cajal body (sca) RNAs, which function as guides for site-specific pseudouridylation of ribosomal and spliceosomal RNAs[8]. Archaeal ACA RNAs contain a single RNA hairpin with a 3' ACA motif, whereas eukaryotic H/ACA RNAs consist of two RNA hairpins hinged by the H-box and flanked by an ACA motif at the 3' end. Each RNA hairpin associates with a heterotetramer of dyskerin, NOP10, NHP2 and GAR1. Mutations in the H/ACA RNP are associated with telomeropathies, notably dyskeratosis congenita (DC) and Hoyeraal-Hreidarsson (HH) syndrome[9], which affect highly proliferating tissues and result in pulmonary and bone marrow abnormalities[2]. High-resolution structural information of these H/ACA RNPs is currently limited to the single-hairpin archaeal and yeast structures[10,11], which cannot rationalize many of these disease mutations.

Structure determination

We collected 43,639 cryo-EM micrographs on a Gatan K3 detector and performed signal subtraction combined with extensive classification[12] to overcome the conformational flexibility of the complex (Extended Data Fig. 1). The resulting reconstructions at 3.4 Å and 3.8 Å resolution for the H/ACA RNP and the catalytic core, respectively, enabled us to build *de novo* atomic models for each lobe (Fig. 1a; Extended Data Figs. 2a-d, 3a-p, 4b-l; Extended Data Tables 1, 2). We performed global classification/refinement to obtain reconstructions for the whole telomerase complex (Extended Data Figs. 1, 2e, f). Multibody refinement[13] revealed that the two lobes adopted multiple conformations relative to each other (Extended Data Figs. 5a-c). We docked the atomic models of the two lobes into these whole telomerase reconstructions combined with DRRAFTER modelling[14] of the RNA linkers between the two lobes (Extended Data Figs. 5d, e). The resulting atomic model for human telomerase holoenzyme consists of hTR, a telomeric DNA substrate and 12 protein subunits: TERT, TCAB1, a histone H2A-H2B dimer, and two copies of the H/ACA

heterotetramer (Figs. 1a-d; Supplementary Data 2, 3). TERT and H2A-H2B form the catalytic core with the pseudoknot/template (PK/t) and conserved regions 4 and 5 (CR4/5) of hTR that are both essential for activity[15] (Figs. 1a-d). The remaining subunits associate with the hTR H/ACA domain, forming the H/ACA lobe (Figs. 1a-d). The two lobes are connected by the P1 and P4.2 stems of hTR (Figs. 1b, d; Extended Data Figs. 5d, e).

Telomerase active site

TERT has four domains: a telomerase essential N-terminal (TEN) domain, a RNA-binding domain (TRBD), a reverse transcriptase (RT) domain and a C-terminal extension (CTE), which is also called the thumb domain (Figs. 1c, 2a-c). As first visualized in *Tetrahymena* TERT[16], the RT domain includes an insertion in the fingers subdomain (named IFD-TRAP) (Extended Data Figs. 6a, b). In the catalytic core, the hTR PK/t (Fig. 1d) encircles TERT domains, forming extensive interactions, mostly through the RNA backbone (Figs. 2b-c). The DNA-RNA duplex is held in the active site (Figs. 2b-c) by interactions with TERT conserved motifs (Extended Data Figs. 3b, 4d, 6a, b). We observed density for the full 3' TTAGGG telomeric repeat of the DNA substrate, which contacts residues in motif T (K570), motif C (L866), thumb loop (S957), thumb helix (residues 970-988), Y949, and R1011 (Fig. 2d; Extended Data Figs. 4e, 6a, 6b, 6d). Previous studies showed that K570E is severely defective in nucleotide addition processivity (NAP) while the thumb mutations L958, L980 and K981 exhibit significant reduction in RAP[17,18]. *Tetrahymena* TERT L813Y mutation (equivalent to human L866) increases RAP and has been proposed to bind DNA[19]. Our structure suggests that these residues are critical for stabilizing the DNA substrate in the telomerase active site. The defects in NAP and RAP induced by these mutations likely result from premature dissociation of the substrate from the active site during repeat synthesis.

The RNA template is embedded within the RT domain (Extended Data Fig. 6e). Although the DNA substrate could theoretically form up to 6 base-pairs with the RNA template, we observed only 4 base-pairs at the AGGG 3' end of the substrate (Figs. 2b, d; Extended Data Figs. 4d, 6c). The preceding TT nucleotides are split away from the template by the CTE domain (Figs. 2b, d). The template base A49 is positioned to base-pair with an incoming dTTP nucleotide, and the 3' hydroxyl of the DNA substrate points towards the catalytic triad (D712, D868, D869 (ref. 5), Extended Data Figs. 3b, 6f). Residue R622 from the finger motif acts as a ratchet to separate A48 from A49, thereby allowing only one template base into the active site at a time (Fig. 2d; Extended Data Fig. 6f). Residues from the RT finger (R631), motif B (Q833) and Y717 are in the vicinity of the vacant nucleotide site (Extended Data Fig. 6f). Structures of the *Tribolium* TERT suggested a role for Y717 as a steric gate that discriminates rNTPs from dNTPs and allows only dNTPs to be incorporated[20]. *Tetrahymena* TERT loses its dNTP/rNTP selectivity when mutated at the equivalent tyrosine (Y623A)[21]. We modelled a dTTP nucleotide[22] that would base-pair with the template A49 in the vacant nucleotide site. A hydroxyl group at the ribose C2 would clash with the side-chain of Y717, suggesting a similar role for Y717 in human TERT (Extended Data Fig. 6g).

TERT interactions with CR4/5 domain of hTR

CR4/5 encompasses the P5, P6 and P6.1 regions of hTR (Fig. 1d), which connect as a three-way junction (Fig. 3a). The P6.1 hairpin is highly conserved in vertebrates, and its duplex length and the two conserved loop nucleotides U307 and G309 are essential for telomerase activity[23,24]. U307 flips out into a hydrophobic pocket of the CTE, and interacts with N1028 (Fig. 3a; Extended Data Figs. 4h). G309 is coordinated by Q1023 and base-stacks with C311 (Fig. 3a). P6.1 is also in close proximity to the P3 stem of the PK/t domain. Strikingly, the bulged U177 in P3 and the flipped-out U307 of P6.1 both interact with L1019 (Fig. 3b; Extended Data Fig. 4i). P5 makes no interactions with TERT, explaining why it is not required for reconstituting telomerase activity in lysates[25]. Although the CR4/5 domain does not directly contact the TERT active site, our structure suggests that, together with the PK/t, it ensures the correct positioning of TERT domains, which is important for telomerase catalytic activity.

Histone H2A-H2B are human telomerase subunits

During 3D classification of the catalytic core, most classes contained an unaccounted density bound to CR4/5 (Extended Data Figs. 1, 7a). This density was unmodelled in our previous 8 Å map (Extended Data Fig. 7b)[3]. Aided by the improved resolution, we performed a molecular replacement search against the BALBES database[26] and obtained histone H2B (PDB 1KX5) (ref. 27) as the top-hit. Fitting of a histone H2A-H2B dimer extracted from a nucleosome structure accounted for the entire density (Extended Data Figs. 3e-h, 7c). Mass-spectrometry analyses of purified telomerase showed the presence of histones H2A, H2B, H3 and H4 (Supplementary Data 4).

As an independent test of this association, we overexpressed telomerase using Twin-Strep TERT and performed 2'-O-Methyl oligo-purification to enrich for hTR (Fig. 3c)[28]. Immunoblotting indicated the presence of H2B, H2A, H3 and H4 in oligo affinity-purified telomerase RNP (O-elution) (Extended Data Fig. 7g). Similar observations were made with endogenous telomerase purified from 293T cells (Extended Data Fig. 7h).

To test whether histone containing telomerase RNPs are active for telomeric repeat synthesis, we further purified telomerase RNPs using histone or Strep-tag antibodies and performed telomerase activity assays and immunoblotting (Figs. 3d, e). Immunoprecipitation (IP) with either H2A or H2B antibodies purified telomerase activity and holoenzyme components (Fig. 3d, lanes 5, 7; 3e), while H3 and H4 antibodies recovered relatively less telomerase activity and components (Fig. 3d, lanes 9, 11; 3e). Compared to TERT Strep-tag IP (Fig. 3d, lane 13), a smaller fraction of input telomerase activity was recovered in association with H2A and H2B (Fig. 3d, lanes 5, 7), consistent with a subset of telomerase holoenzyme particles having homogenous density for H2A-H2B. H3 and H4, which are not observed in the density of analyzed particle classes, are either absent or associated with the holoenzyme but are too flexible to contribute to observable densities.

H2A-H2B binds to the three-way junction across the P5 and P6.1 stems, using the same positively charged H2A-H2B surface that binds nucleosomal DNA (Fig. 3a; Extended Data

Figs. 7d, e). Consistent with our model, purified recombinant human H2A-H2B dimer bound CR4/5 in native gel assays (Fig. 3f; Extended Data Figs. 7f, k). Recent work emphasizes that CR4/5 alone adopts heterogeneous conformations[29]. In holoenzyme particles, CR4/5 adopts a more homogenous conformation. Together, these findings suggest that the histone H2A-H2B heterodimer may act to stabilize and/or position the CR4/5 fold during telomerase RNP assembly in cells. This would explain why active human telomerase is not readily reconstituted from purified TERT and hTR but can be assembled by co-expression of TERT and hTR *in vivo*.

The H/ACA RNP structure

The first high-resolution structure of a complete eukaryotic H/ACA RNP presented here reveals numerous molecular interactions that were not possible to infer from previous single-hairpin archaeal and yeast RNP structures[10,11]. The double-hairpin H/ACA RNA scaffolds the assembly of two copies each of dyskerin, NHP2, NOP10 and GAR1, one on each hairpin (Fig. 4a; Extended Data Figs. 8a, 8b). For clarity, we describe the components of the assemblies bound to the 5’ and 3’ hairpins as 5’ and 3’, respectively (Fig. 4a).

The conserved H- and ACA-boxes are brought into close proximity by the two dyskerin molecules (Fig. 4a; Extended Data Figs. 3p, 4k, 8a, 8c). The AGA motif of the H-box (ANANNAA) and the ACA-box form similar interactions with the 5’ and 3’ dyskerin molecules, respectively (Extended Data Fig. 8c). Unexpectedly, the conserved H-box A377 and ACA-box C447 form van der Waals and stacking interactions with each other and with the 3’ dyskerin (Extended Data Fig. 4k, 8c). These cross-hairpin interactions distinguish eukaryotic H/ACA two-hairpin RNPs from their predecessor archaeal ACA single-hairpin RNPs.

The P8b hairpin (Fig. 4a; Extended Data Fig. 8a) makes unique contributions to hTR cellular accumulation and localization[30,31]. The apical hairpin loop contains two motifs: a conserved ugAG sequence (CAB-box), which binds the Cajal body localization factor, TCAB1 (ref. 32-34), and a biogenesis-promoting (BIO) box that enhances hTR 3’ hairpin assembly as a H/ACA RNP[31] (Extended Data Figs. 3o, 8b, 8d). Of note, the CAB-box is recognized by both TCAB1 and NHP2 (Fig. 4a; Extended Data Fig. 3o, 8d). Loop G412 and G414 form -stacking interactions, supported by the coordination of R387 and a number of hydrophobic residues of TCAB1 to G414 (Extended Data Fig. 4l, 8d). This purine-purine stacking positions G414 and A413 for interactions with TCAB1. A413 and G414 have been shown to promote Cajal body localization, and the G414C mutation is sufficient to abolish TCAB1 association with telomerase holoenzyme[32]. The G414 to C mutation could destabilize this stacking structure and hence hTR interaction with TCAB1.

The positioning of the CAB-box 3’ loop region is assisted by the BIO-box. The conserved U418 within the BIO-box flips out and interacts with K111 and L86 of NHP2 (Extended Data Fig. 8d). Despite being required for Cajal body localization, the CAB-box is dispensable for hTR accumulation[30,35]. However, the BIO-box U418C mutation strongly disrupts hTR accumulation[31]. The observed interaction between the BIO-box and NHP2 explains the enhanced affinity of telomerase 3’ H/ACA hairpin for H/ACA proteins and

suggests that NHP2 binding to the P8b hairpin could stabilize or remodel the loop for TCAB1 binding.

Disease mutations in the H/ACA RNP

We modelled parts of the poorly characterized N- and C-termini of both dyskerin molecules, which were either were unresolved or adopted different conformations in previous structures [10,11]. A 5' dyskerin N-terminal extension (residues 36-55) sits in the 3' dyskerin hydrophobic pocket formed by the N-terminal region and the PUA domain (Figs. 4b, c; Extended Data Fig. 3m). The equivalent hydrophobic pocket of the 5' dyskerin subunit seats a helix (residues 352-357) of the 3' dyskerin (Figs. 4b, d; Extended Data Fig. 3n). The N-terminal extension and this hydrophobic pocket of dyskerin harbor the majority of the DC and HH mutations[9] (Fig. 4b). These mutations likely disrupt the reciprocal dyskerin-dyskerin interactions and thus telomerase RNP assembly. Most remaining disease mutations map to other important protein-protein and protein-RNA interfaces (Fig. 4b). In light of our structure, native telomerase H/ACA RNP assembly would rely on a combination of increased H/ACA protein affinity for the 3' H/ACA RNA hairpin, afforded by NHP2, and cross-hairpin dyskerin interactions.

Discussion

The structure reported here not only provides unparalleled insights into the human telomerase active site, but also surprising new clues about requirements for RNP biogenesis and a new role for histone proteins beyond the nucleosome.

Multiple repeat synthesis activity necessitates that human telomerase undergoes a complex catalytic cycle, involving the translocation of the nascent DNA product and its realignment with the template region of hTR[17,36] (Extended Data Fig. 6c). After dissociation from the template, the nascent DNA product is retained to allow rebinding of the DNA 3' end to the alignment region of the template (Extended Data Figs. 6c, l). To achieve DNA product retention, non-template single-stranded DNA binding interface(s) are described as an "anchor point" during catalysis[17 37]. In our structure, the enzyme is bound to a 3' TTAGGG repeat, prepared for incoming dNTP binding (Extended Data Fig. 6c). The structure reveals an extensive DNA binding surface around the active site predominantly formed by the T-motif and the thumb CTE domain (Fig. 2d; Extended Data Fig. 6d). Our structure also shows a positively charged surface at the human IFD-TRAP-TEN interface that could potentially guide DNA away from the active site (Extended Data Figs. 6h-j) and provide an anchor point for the DNA substrate (Extended Data Figs. 6l).

In human cells, telomerase is recruited to telomeres by TPP1-POT1, components of the shelterin complex, *via* interactions between TPP1 and the TERT TEN domain[38-41]. We modelled TPP1-POT1 bound to the human TEN domain using the analogous *Tetrahymena* p50-TEB complex[16]. The role of p50-TEB complex in telomerase recruitment and activation in *Tetrahymena* has been proposed to parallel that of TPP1-POT1 in human[42,43]. The proposed DNA path would bring the product DNA close to POT1 single-stranded DNA binding domains in this TPP1-POT1 model (Extended Data Figs. 6i-k).

We discovered a novel role for the histone H2A-H2B heterodimer as an RNA binding factor for hTR CR4/5. Our structure suggests that H2A-H2B functions in human telomerase to perform a similar role similar to that of the La-family *Tetrahymena* telomerase holoenzyme protein p65 (ref. 44). p65 binds to *Tetrahymena* stem-loop 4, which has somewhat similar structural placement to CR4/5 P6.1 stem-loop in telomerase catalytic core, to stabilize a TER conformational change that promotes TERT-TER interactions[45] (Extended Data Figs. 7i, j). Superimposition of the histone octamer, with flexible tails removed, on H2A-H2B in telomerase catalytic core results in very little clash and therefore may be compatible with H3-H4 binding (Extended Data Fig. 7l). Telomerase has been proposed to associate with the replication fork to account for replication-coupling of telomerase action at telomeres[46,47]. After replication fork passage, H3-H4 tetramers are deposited on the daughter DNA free of H2A-H2B[48]. It is tempting to speculate that the H2A-H2B heterodimer within the telomerase holoenzyme plays a role in recruiting telomerase to chromosome ends specifically post-replication, *via* interactions with replication-coupled deposition of H3-H4 tetramers. Furthermore, H2A-H2B availability for hTR interaction could regulate the assembly or telomere recruitment of active telomerase holoenzyme across the cell cycle.

Methods

Telomerase purification

Human telomerase was reconstituted in HEK 293T cells by co-expression of a TERT expression plasmid (pcDNA 3.1-ZZ-Tev-Twin Strep-TERT or pcDNA 3.1-Twin Strep-TERT) and pcDNA 3.1-U3-hTR-HDV. Tev is a Tobacco Etch Virus protease cleavage site, and HDV is the hepatitis delta virus ribozyme. Human telomerase-DNA substrate ($T_{12}T_2AG_3$) complex used for cryo-EM was purified as described previously[3]. Briefly, whole-cell extracts were prepared from transfected 293T cells by three freeze-thaw cycles. Extracts from 120-160 plates of cells were incubated with streptavidin agarose resin (Sigma-Aldrich) pre-bound to a 5'-biotinylated 2'-O-Methyl oligonucleotide at room temperature for 3 hours. The resin was then washed with wash buffer (20 mM HEPES NaOH pH 8.0, 150 mM NaCl, 2 mM $MgCl_2$, 0.2 mM EGTA, 10% glycerol, 0.1% Igepal CA-630, 1 mM DTT) and eluted with a competitor oligonucleotide. The eluate was incubated with MagStrep XT resin (IBA LifeSciences) overnight at 4 °C. The resin was washed with wash buffer and eluted in batch with biotin elution buffer (100 mM Tris HCl pH 8.0, 150 mM NaCl, 1 mM EDTA, 5-10 mM biotin, 2 mM $MgCl_2$, 0.1% Igepal CA-630, 10% glycerol, 1 mM DTT). The complex for structural determination has a ZZ-Tev-Twin-Strep tag on TERT. For the histone experiments, we used a Twin-Strep-TERT construct to avoid binding of the ZZ-tag on IgG sepharose. Endogenous telomerase was purified from whole-cell extracts prepared from HEK 293T cells using the 2'-OMethyl oligonucleotide purification as described above. HEK 293T cell lines were obtained from ATCC (ATCC® CRL-3216™) and exhibited the expected morphology and growth. They have not been authenticated or tested for mycoplasma recently.

Mass spectrometry

Purified telomerase was analyzed by tandem mass spectrometry. Supplementary Data 4 shows full mass spectrometry results.

Histone immunoprecipitation

Whole cell extract from HEK 293T cells transfected with Twin-Strep-TERT and hTR expression constructs was subjected to 2'-O-Methyl oligo-purification using a 5'-biotinylated 2'-O-Methyl oligonucleotide, which can hybridize with hTR template region as described above[28,49]. The sample was eluted using a competitor oligonucleotide. 25 μl Magnetic protein A/G sepharose beads (Pierce), pre-bound to α-H2A, α-H2B, α-H3, α-H4 or α-Strep or no antibody (negative control), were incubated with 100 μl eluate overnight at 4 °C. All histone antibodies used were ChIP-grade. The flow-through was collected for western blot (15 μl) and activity assays (5 μl). The beads were washed three times with wash buffer (20 mM HEPES NaOH pH 8.0, 150 mM NaCl, 2 mM $MgCl_2$, 0.2 mM EGTA, 10% glycerol, 0.1% Igepal CA-630, 1 mM DTT) and resuspended in wash buffer. 5 or 25% of the resuspended beads were subjected to telomerase activity assays, and 25% of the beads were boiled in SDS-loading buffer for SDS-PAGE and immunoblotting.

Telomerase activity assays

Telomerase primer extension assays were performed in 20 μl reactions containing 50 mM Tris-acetate pH 8.0, 4 mM $MgCl_2$, 5 mM DTT, 250 μM dTTP, 250 μM dATP, 5 μM unlabelled dGTP, 0.1 μM α-^{32}P dGTP (3000 Ci/mmole, 10 mCi/ml, Perkin Elmer), 500 nM $(T_2AG_3)_3$. The reactions were performed at 30 °C for 40 min, stopped with 50 mM Tris HCl pH 7.5, 20 mM EDTA, 0.2 % SDS,extracted with phenol:chloform:isoamyl alcohol and precipitated with ethanol and a 12-nt ^{32}P labelled $(T_2AG_3)_2$ oligonucleotide. The products were resolved on a 10.5% denaturing polyacrylamide TBE gel, which was dried and exposed to a phosphorimager screen. The screen was scanned using an Amersham Typhoon Biomolecular Imager (Cytiva). Bands were quantified using ImageQuant (Cytiva).

Immunoblotting

Samples were resolved on a 4-12% Bis-Tris SDS-PAGE gels and transferred onto a nitrocellulose membrane. The membrane was blocked with 5% non-fat milk in phosphate saline buffer (PBS) supplemented with 0.1% Tween-20 (PBST) for 1 hour and incubated with primary antibodies overnight at 4 °C. It was then washed with PBST, incubated with secondary antibodies (Abcam) in 5% non-fat milk for 1 hour and washed again with PBS before being imaged on a Li-COR Odyssey imager. The primary antibodies used were rabbit α-H2A (1:250, Cell Signaling Technology), rabbit anti-H2B (1:1000, Abcam), rabbit anti-H3 (1:1000, Abcam), mouse anti-H4 (1:1000, Cell Signaling Technology), rabbit α-NHP2 (1:1000, Proteintech), rabbit α-NOP10 (1:1000, Abcam), rabbit α-dyskerin (1:500, Santa Cruz Biotechnology), rabbit α-Strep (1:500, Genscript). All histone antibodies used were ChIP-grade. The secondary antibodies used were goat α-rabbit Alexa-Fluor 680 or 790 (1:5000, Abcam) and goat α-mouse Alexa-Fluor 680 (1:5000, Abcam). Densitometry for quantification was performed in ImageJ.

Human H2A-H2B purification

Human histone H2A-H2B dimer was purified as described with modifications[50]. Bacterial codon optimized H2A and H2B with N-terminal His6-HRV-3C site fusions were individually expressed as inclusion bodies. HRV-3C is human rhinovirus 3C protease

cleavage site. 2 L of transformed BL21 Star(DE3) cells were cultured at 37 °C in 2xTY media supplemented with 50 μg/ml kanamycin and 35 μl/ml chloramphenicol to OD_{600} = 0.6, then induced with 1.0 mM IPTG followed by a 3 hour incubation at 37 °C. Harvested cells were resuspended in 50 ml wash buffer (50 mM Tris-HCl pH 8.0, 100 mM NaCl, 1 mM EDTA, 1mM PMSF) supplemented with EDTA-free protease inhibitors (Roche) and frozen at -20 °C to lyse. Lysates were thawed, sonicated to reduce viscosity, and centrifuged for 20 min at 4 °C and 25,000*g*. The pellet was washed by resuspension in wash buffer supplemented with 1% (v/v) Triton X-100, and spun for 10 min at 4 °C and 12,000 rpm. This was repeated twice more with wash buffer. The pellet was extracted in unfolding buffer (7.0 M urea, 50 mM Tris-HCl pH 8.0, 0.5 M NaCl, 30 mM Imidazole, 0.1% Igepal CA-630, 1 mM DTT, 1 mM PMSF), centrifuged to remove insoluble material, then applied to a 5 ml HisTrap HP column (Cytiva) in buffer A (6.0 M urea, 50 mM Tris-HCl pH 8.0, 0.5 M NaCl, 30mM Imidazole, 1 mM DTT, 1 mM PMSF). The column was washed with 30 column volumes (CV) of buffer A and step eluted to 100% buffer A supplemented with 500 mM imidazole. H2A and H2B were mixed at equimolar ratios and adjusted to a concentration of 1 mg/ml then refolded by extensive dialysis against refolding buffer (50 mM Tris-HCl pH 8.0, 2 M NaCl, 1 mM EDTA, 1 mM DTT). The final dialysis was performed overnight. The next day dialysate was concentrated using a 10,000 MWCO Amicon centrifugal concentrator (Millipore) and further purified using a Superdex200 Increase 10/300 size exclusion column (Cytiva) in SEC buffer (50 mM Tris-HCl pH 8.0, 2 M NaCl, 1 mM EDTA, 1 mM DTT). Peak fractions were pooled, concentrated, checked for RNase contamination, aliquoted, flash frozen in liquid nitrogen and stored at -80 °C prior to use.

In vitro transcription and RNA purification

Transcription was performed using a linearized plasmid template of CR4/5. Each transcription reaction was composed of 4 mM of each of ATP, CTP, GTP and UTP, 50 mM Tris HCl pH 8.0, 1 mM spermidine, 10 mM DTT, 30 mM $MgCl_2$, 15 μg/mL T7 polymerase and 100 μg/mL linearized plasmid. The reaction mixture was incubated at 37 °C overnight and spun at 5000 rpm for 10 min to remove magnesium pyrophosphate precipitate. The supernatant was diluted with the same volume of water and precipitated with 6 volumes of ethanol at -20 °C overnight. The precipitated RNA was resuspended in formamide dye and run on an 8% denaturing acrylamide TBE gel with 7 M urea. The RNA band was excised from the gel using UV shadowing. For small-scale preparation, the RNA was extracted from the gel pieces by rotating them in crush and soak buffer (500 mM ammonium acetate, 1 mM EDTA, 0.5% SDS) overnight at 37 °C. The gel pieces were removed by filtration. The RNA was phenol/chloroform extracted twice then precipitated overnight at -20 °C in 2.5 volumes of ethanol. The RNA pellet was resuspended in TE, aliquoted and stored at -80 °C until use.

Electrophoretic mobility shift assays

5’ ^{32}P-radiolabeled CR4/5 was refolded by heating to 95 °C for 5 min in TE supplemented with 2 mM $MgCl_2$, then allowed to cool to room temperature overnight. Increasing concentrations of H2A-H2B dimer (0.25 - 20 pmol) were incubated with 1 fmol radiolabeled CR4/5 on ice in a total volume of 10 μl EMSA buffer (50 mM Tris-HCl pH 8.0, 250 mM NaCl, 1 mM $MgCl_2$, 100 μg/ml BSA, 25 μg/ml T11 RNA[51], 0.5 mM DTT). After 1 hour, Ficoll was added to a final concentration of 2.5 % and each sample was resolved by

electrophoresis on a 5% native 37.5:1 polyacrylamide gel at 4 °C in 0.5XTBE, dried and visualized with phosphorimaging. Bands were quantified with ImageQuant (Cytiva) and analyzed with Prism 8 using a single-site saturation binding model (GraphPad)[52].

Cryo-EM electron microscopy

For cryo-EM data collection, we applied 3 μl of purified human telomerase on a C-flat-T-50 4/2 grids (Protochips) which were precoated with a layer of ~5-6-nm thick homemade continuous carbon film and glow-discharged using a Sputter coater discharger (model Edwards S150B). The grids were blotted for 5s at 100% humidity and 4 °C and vitrified in liquid ethane using an FEI Vitrobot MK IV. Data collection was performed on an in-house ThermoFisher Titan Krios transmission electron microscope operated at 300 kV and equipped with a Gatan K3 direct electron detector camera and a GIF Quantum energy filter. Images were collected automatically using the Serial-EM package[53] in counting mode with a physical pixel size of 1.11 Å/pixel, with a total electron dose of 47 electrons per $Å^2$ during a total exposure time of 2.49 s, dose-fractionated into 48 movie frames (Extended Data Table 1). We used a slit width of 20 eV on the energy filter and a defocus range of 1.2-3.5 μm. A total of 43,693 micrographs were collected from two separate sessions.

Image processing

Most steps of data processing were done in RELION 3.1 (ref. 54) unless otherwise stated (Extended Data Figs. 1, 5a). The movies for each micrograph were first corrected for drift and dose-weighted using RELION. Contrast transfer function (CTF) parameters were estimated for the drift-corrected micrographs using CTFFIND4 within RELION[55]. The two datasets were first processed separately and combined at a later stage.

For the first dataset, we rescaled the good 2D class averages from the previous dataset collected with a K2 camera[3] and used them as references for auto-picking. These particles were binned by 4 and extracted with a box size of 100^2 pixel for 3D classification. Particles from the best 3D class was unbinned and subjected to a round of 2D classification. The best 2D class averages from this 2D classification were then used for the second round of auto-picking. A total of 8,401,685 particles were picked, binned by 4 and extracted with a box size of 100^2 pixel. We performed 3D classification of these particles with 8 sub-classes, angular sampling of 15°, regularization parameter T of 4 and an initial model from our previous published dataset. We selected 3D classes with intact H/ACA lobe and catalytic core and ran reference-free 2D classification to remove any remaining bad particles and contaminants. The resulting 1,853,803 particles with two intact lobes were un-binned and refined to yield an 8.1 Å reconstruction. As expected, this reconstruction does not show secondary structural features expected at this resolution due to the conformational heterogeneity between the two lobes. We divided the structure into the H/ACA lobe and the catalytic core and performed signal subtraction with recentering to obtain particle images containing and centered at just the lobe of interest. We also downsized the box size of the H/ACA lobe and the catalytic core to 240^2 pixel and 180^2 pixel, respectively during this process to speed up downstream processing. For each lobe, three rounds of 3D classification into 6 classes were run for 25 iterations each round with angular samplings of 15°, 7.5° and 3.75°, respectively. The best class for the H/ACA lobe consisting of 591,197 particles was

refined to 3.9 Å resolution. They were subsequently reverted to the original particles for Bayesian polishing. The polished particles were refined and signal subtraction with recentering was performed again to remove the density from the catalytic core. We refined the signal-subtracted polished particles to 3.9 Å resolution and used the angular assignments from this refinement for alignment-free 3D classification. A subset of 98,663 particles from the best 3D class was selected and refined to 3.7 Å resolution. For the catalytic core, a subset of 888,369 particles from the best two classes were selected and refined to 4.1 Å. They were reverted to the original particles for Bayesian polishing. The refined polished particles were subjected to signal subtraction with recentering to remove the density from the H/ACA lobe. They were then refined to 4.3 Å. Another round of alignment-free 3D classification was performed to resolve further heterogeneity. A subset of 133,816 particles from the best class was selected and refined to 4.1 Å resolution. The best subsets for each lobe were later combined with the best subsets of particles from the second dataset.

For the second dataset, 2D references from the first dataset were used for auto-picking, resulting in 7,358,749 picked particles. We employed a similar strategy as the first dataset with 3D classification followed by 2D classification to yield 1,865,927 particles, which were unbinned and refined to 6.7 Å. We performed signal subtraction and applied similar classification/refinement strategies as in the first dataset for the individual lobes. For the catalytic core, we obtained a subset of 34,722 particles, which were refined to 4.2 Å resolution. For the H/ACA lobe, we also applied similar strategies, except Bayesian polishing did not improve the reconstruction. A best subset of 106,002 particles was refined to 3.6 Å resolution.

We combined the best subsets of particles from the two datasets for each lobe. The combined subset 168,538 particles for the catalytic core was refined to 3.9 Å resolution. Beam-tilt and defocused refinement further improved the reconstruction to 3.8 Å resolution[56]. 204,665 particles for the H/ACA lobe were refined to 3.6 Å, which was improved to 3.4 Å with beam-tilt and defocused refinement.

To obtain the reconstruction of the whole complex containing both lobes, we combined the 1,853,803 particles from the first dataset and the 1,865,927 particles from the second dataset prior to signal subtraction and performed 3D classification at bin4 (Extended Data Fig. 1). The best two subsets were unbinned and refined. The first subset of 484,847 particles (3D class 2) was refined to 4.5 Å. However, this reconstruction exhibited preferential orientation in the H/ACA lobe. The second subset of 463,013 particles (3D class 5) was refined to 6.6 Å. For both subsets, the H/ACA lobe was better aligned than the catalytic core, and the resulting maps were heterogenous in resolution, indicative of a high degree of conformational heterogeneity (Extended Data Figs. 2e, f).

To analyze the conformational dynamics within each of these two subsets, we performed multi-body refinement on each of the subsets using two masks for the H/ACA lobe and the catalytic core (Extended Data Figs. 5a-c). This was followed by principal component analysis using 6 eigenvectors to identify the motions between the two lobes[13]. The first subset was refined to 3.9 Å and 10.3 Å resolution for the H/ACA lobe and the catalytic core, respectively. The second subset was refined to 4.3 Å and 9.3 Å resolution for the H/ACA

lobe and the catalytic core, respectively. The two extreme states in each volume series for the first 6 principal components were shown in Extended Data Figs. 5b and c and clearly illustrated the conformational flexibility between the two lobes.

All refinements were performed using fully independent data half-sets and resolutions are reported based on the Fourier shell correlation (FSC) = 0.143 criterion[57,58] (Extended Data Fig. 2a). FSCs were calculated with a soft mask. Maps were corrected for the modulation transfer function of the detector and sharpened by applying a negative B-factor as determined either by the post-processing function of RELION or by a user-defined value. Local resolution was calculated within RELION (Extended Data Figs. 2c-f).

H2B identification by molecular replacement

To identify the previously unassigned density, we located the center of mass of the density using COOT and use a map within a 30 Å radius from this center of mass for molecular replacement search against BALBES database using MolRep[26,59,60]. The search returned H2B (PDB 1KX5, chain D[27]) as the top hit with a contrast score of 3.90 with excellent fit. Other top hits with contrast scores above 3 showed poor fits. The H2A-H2B dimer extracted from the nucleosome structure (chains C and D, PDB 1KX5) showed perfect fit in our unassigned density.

Model building and refinement

All model building was performed *de novo* in COOT[61] using the placement of the homology models of the 8 Å structure[3] in the 3.4 Å and 3.8 Å maps of the H/ACA lobe and the catalytic core, respectively. To aid modelling building, we converted the maps to MTZ format using REFMAC5.8, which can be blurred and sharpened in COOT[59]. We first built the RNA manually. For hTR in the catalytic core, we used DRRAFTER to model regions that were more ambiguous (see below for more details)[14]. The top 10 scoring models from DRRAFTER were manually inspected for fitting in the maps. The best fit models for each region were incorporated into the manually built RNA coordinates. We further improved RNA geometry for hTR in both lobes using ERRASER[62]. The resulting models were fixed manually to remove clashes with the protein models prior to model refinement. Extended Data Table 2 summarizes the modelled components. The models were refined first in real-space using Phenix[63] and then in reciprocal space using REFMAC5.8[64] with protein secondary structure restraints calculated using PROSMART[65] and RNA base-pair and stacking restraints using LIBG[59]. FSC model versus map was calculated using Phenix (Extended Data Fig. 2b)[63]. The geometries of the refined models were analyzed by MolProbity[66]. A summary of deposited maps, models and refinement statistics are provided in Extended Data Table 1. As an additional validation of the RNA register assignment, we shifted the registers of important RNA regions including the template, CAB-box, H- and ACA-boxes in the refined models by one residue and calculated model-to-map cross-correlations (CC) for these alternative models using Phenix[63]. As expected, these models show poorer CC compared to our final refined models (Supplementary Table 1).

DRRAFTER modelling of hTR

For the hTR region in the catalytic core, the density map allowed for manual tracing of positions 32-36, 46-56, 64-67, 79-83, 89-131, 142-150, 163-192, 242-246, 256-273, 282-317, and 322-327. DRRAFTER[14] was used to model the remaining nucleotides (18-31, 37-45, 57-63, 68-78, 84-89, 132-142, 195-208, 234-241, 247-255, 274-281, 318-324, and 328-337). Protein density was subtracted from the map by removing a 3 Å zone around protein residues with Chimera, and the map was low-pass filtered to 4 Å with EMAN2 (ref. 67). Manually built RNA residues and all protein coordinates in the catalytic core were included as a single rigid body during modelling. Additionally, A-form helices for P1a (18-31 and 195-208), P2a.1 (68-72 and 136-140), and P4 (234-240 and 331-337) were included as rigid bodies. The ten top-scoring models have a convergence (mean pairwise RMSD) of 4.54 Å, yielding an estimated RMSD accuracy of 4.57 Å for residues modeled with DRRAFTER. These ensembles are included in Supplementary Data 1.

For the full-length maps, hTR residues that were built using the high-resolution density for each lobe separately above were fit as rigid bodies into the lower-resolution full-length classes 2 and 5 dual-lobe maps (Extended Data Figs. 1, 2 and 5a) using Chimera and Coot. For the catalytic core, all protein residues and hTR residues 38-150, 163-186, 256-261, and 295-315 were fit, and for the H/ACA domain, all protein residues and hTR residues 211-218, 362-392, and 397-449 were fit. Coordinates for helix P6b were not included at this stage, as the fitted position did not match the density for this helix in the dual-lobe maps. A 5 Å zone of density around the fitted coordinates was subtracted with Chimera, and the resulting map was segmented using Chimera's Segment Map tool; segments were selected to preserve density for only helix P6b and the hTR linker. DRRAFTER was used to model helix P6b and the hTR linker (residues 18-37, 187-210 219-255, 316-362). Fitted catalytic core and H/ACA domain coordinates were included as a rigid body during modeling. Additionally, A-form helices were included as rigid bodies for P1a (18-31 and 195-208), P4.1 (225-231, 341-344, and 346-348), P4.2 (234-240 and 331-337), P5 (243-247 and 322-326) and P6b (268-275, 280-284, and 286-288). For models built into class 2, the ten top-scoring models have a convergence of 8.63 Å for helix P6b and the hTR linker stems (P4.2 and P1, Fig. 1d), yielding an estimated RMSD accuracy of 8.54 Å for these regions (Extended Data Fig. 5d; Supplementary Data 2). For models built into class 5, the ten top-scoring models have a convergence of 10.58 Å for helix P6b and the hTR linker stems (P4.2 and P1, Fig. 1d), yielding an estimated RMSD accuracy of 10.43 Å for these regions (Extended Data Fig. 5e; Supplementary Data 3).

Map and model visualization

The signal subtracted maps for the catalytic core and the H/ACA lobe were recentered at the center of each individual map. Therefore, for illustrations in Fig. 1, we fitted them to the full 3D class 2 map (Extended Data Fig. 5). Maps were visualized in Chimera and ChimeraX[68,69] and all model illustrations were prepared using either Pymol (www.pymol.org) or Chimera.

Europe PMC Funders Author Manuscripts

Extended Data

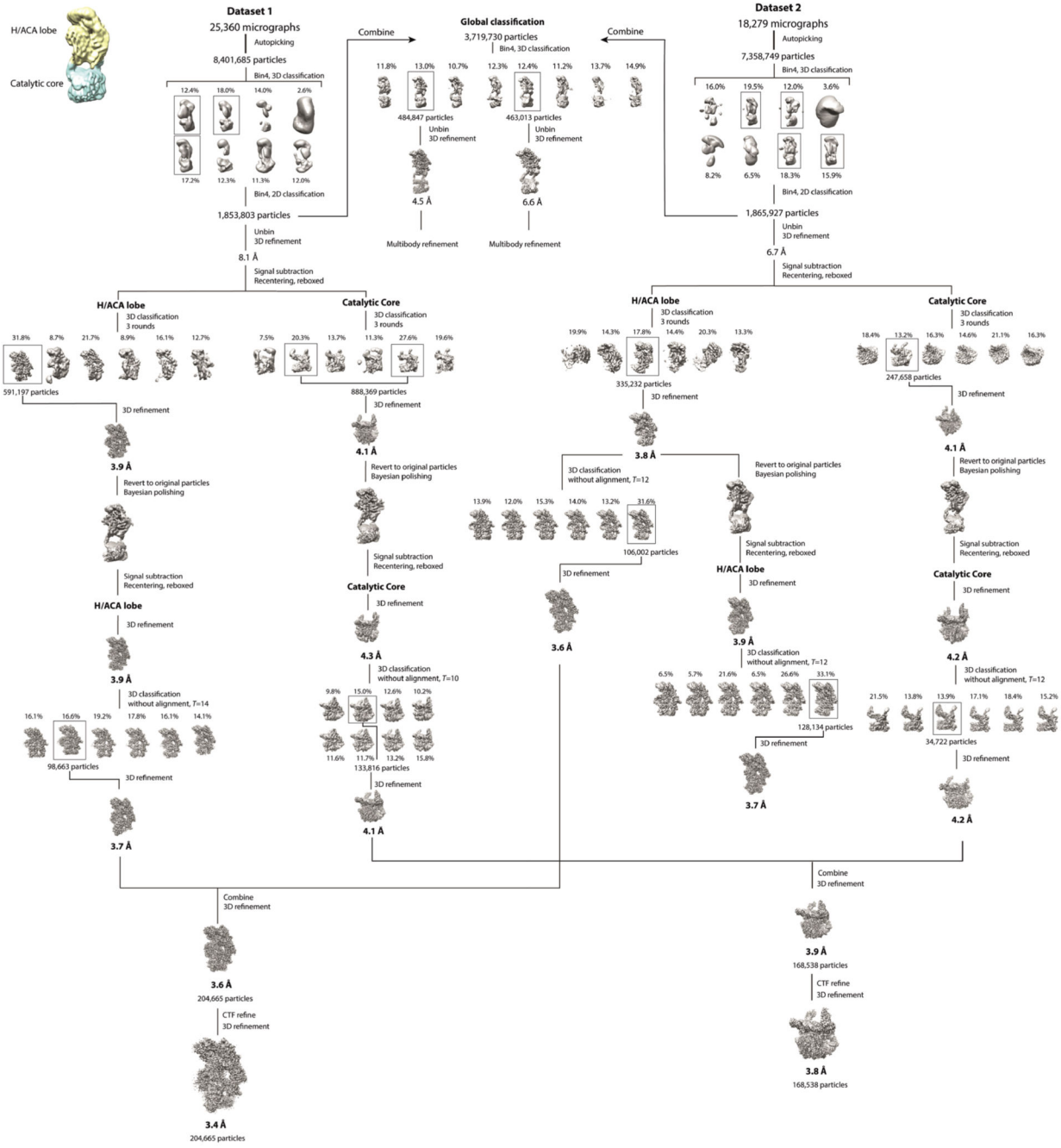

Extended Data Figure 1. Image processing scheme.

Summary of the data processing strategies that yielded the reconstructions described in this study.

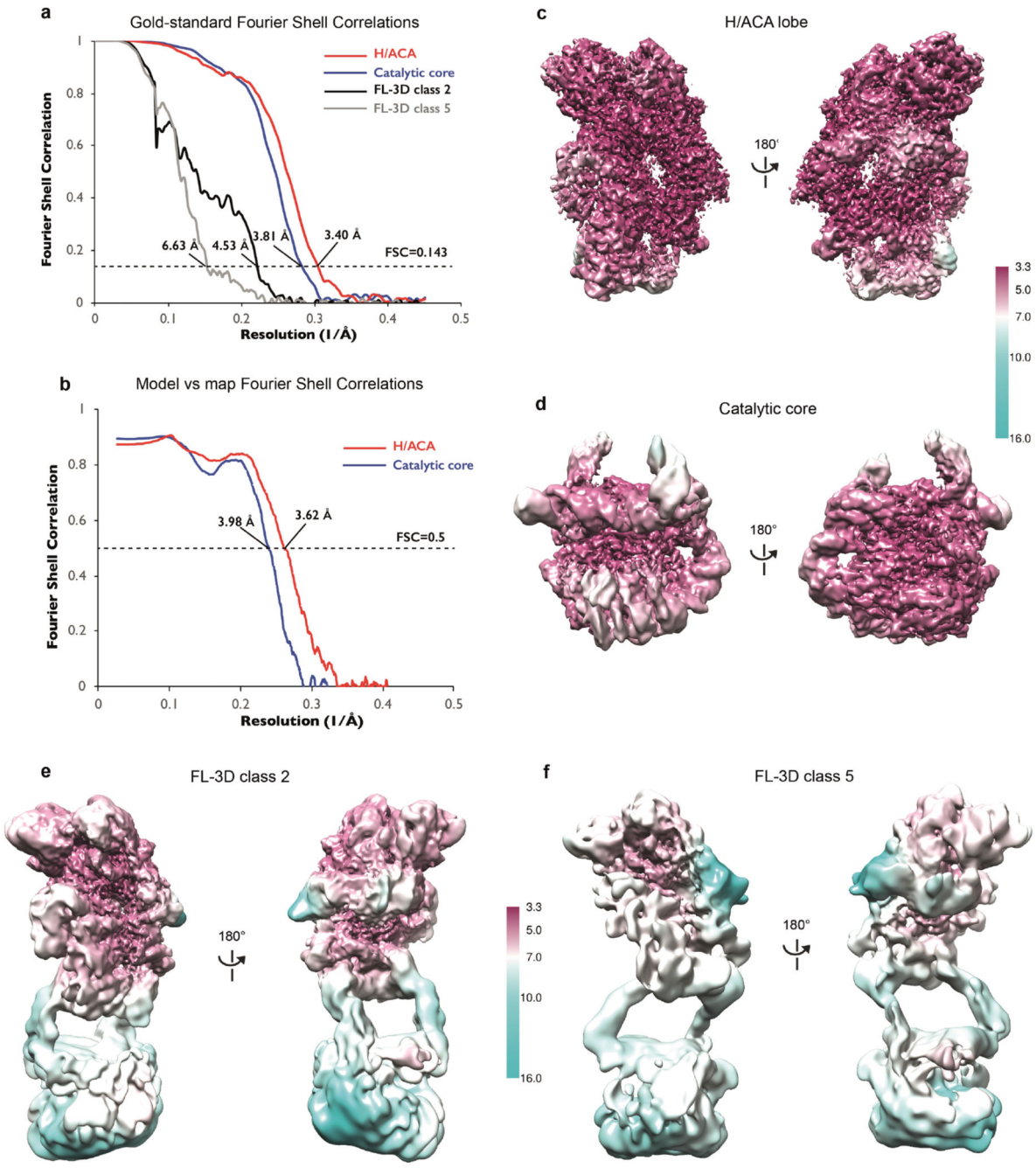

Extended Data Figure 2. Local resolution and resolution estimation.

a, Gold-standard FSC curves for maps of H/ACA lobe, the catalytic core and the best two full-length (FL) classes. Resolutions were estimated at FSC=0.143. **b**, FSC curves for the refined H/ACA and catalytic core models vs the corresponding maps. Resolutions were estimated at FSC=0.5. Local resolution estimated by RELION 3.1 (ref. 54) for **c**, the H/ACA lobe; **d**, the catalytic core; **e**,FL-3D class 2; **f**, FL-3D class 5. For direct comparisons, the same local resolution range (3.3-16 Å) was used for all maps.

Europe PMC Funders Author Manuscripts

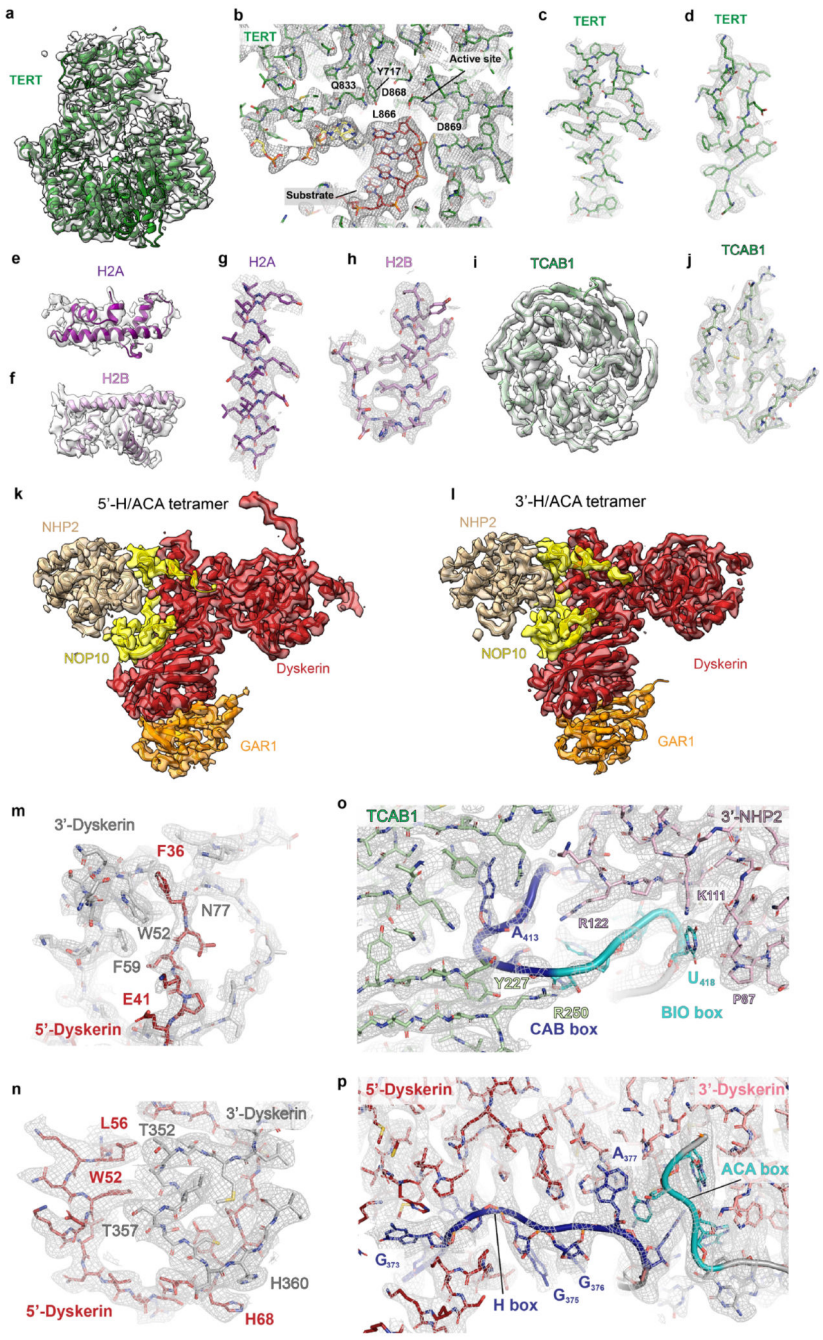

Extended Data Figure 3. EM density of protein components.

Full densities of **a**, TERT; **e**, histone H2A; **f**, histone H2B; **i**, TCAB1; **k**, 5' H/ACA tetramer; **l**, 3' H/ACA tetramer. **b**, Close-up view of the active site density of TERT with an empty nucleotide binding pocket (see also Extended Data Fig. 6f). **c, d**, Representative EM densities of TERT. **g**, **h**, **j**, Representative EM densities of histone H2A, histone H2B and TCAB1, respectively. **m**, Close-up view of the density of N-terminal extension of the 5'-dyskerin bound to a hydrophobic pocket within the 3'-dyskerin (see also Fig. 4c). **n**, Close-up view of the density of helix 352-375 of the 3'-dyskerin bound to the equivalent

hydrophobic pocket as in panel (**m**) within the 5'-dyskerin (see also Fig. 4d). **o**, Close-up view of the density of hTR P8 stem loop containing the CAB- and BIO-boxes, which interact TCAB1 and the 3' NHP2 (see also Extended Data Figs. 4l and 8d). **p**, Close-up view of the density of the H- and ACA-boxes interacting with the two dyskerin molecules (see also Extended Data Figs. 4k and 8c).

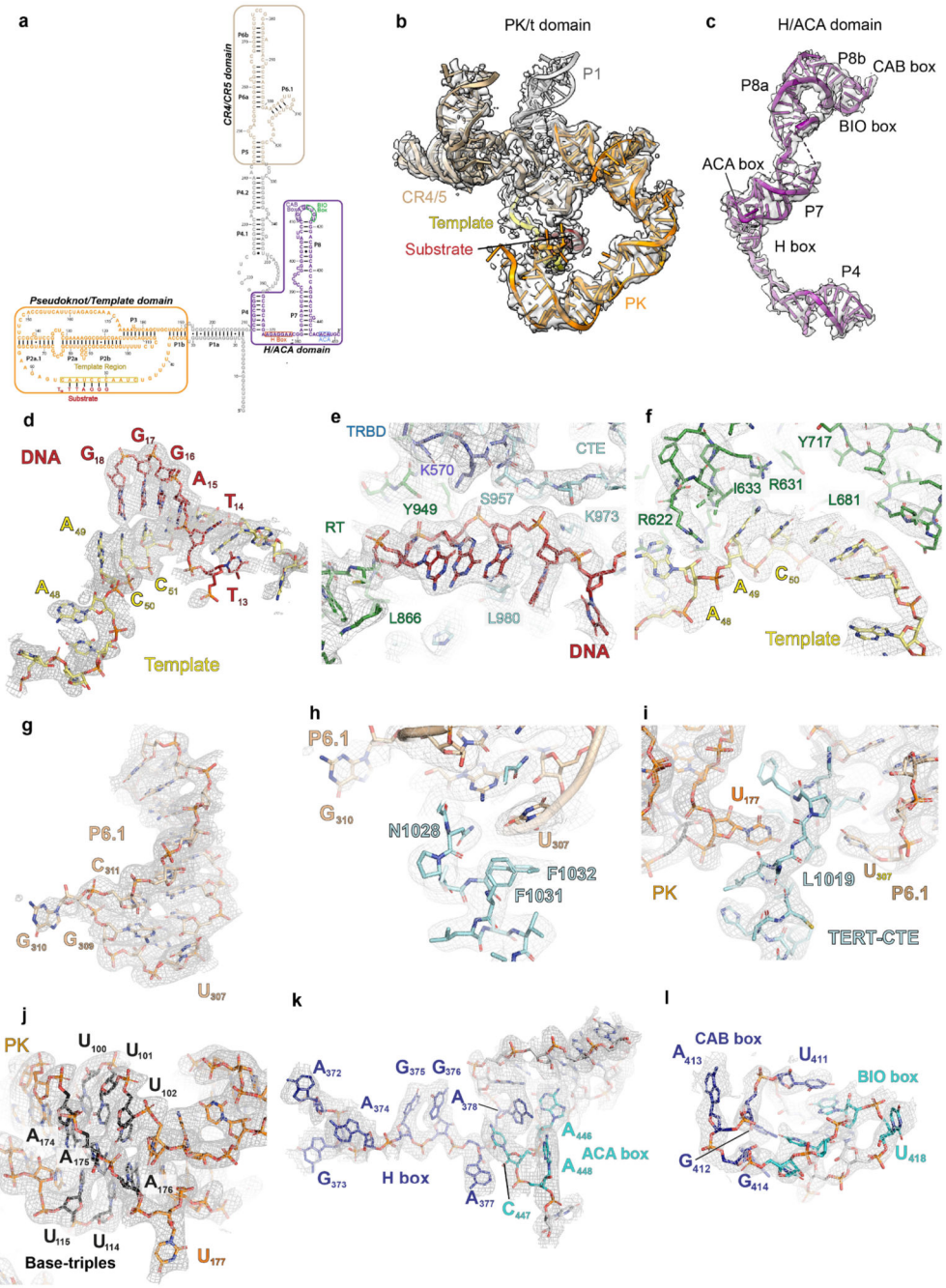

Extended Data Figure 4. EM density of hTR and DNA substrate.

Europe PMC Funders Author Manuscripts

a, Secondary structure schematic of hTR based on the structure. This figure was modified from the telomerase database[70]. **b**, **c**, Full density of hTR in the catalytic core and the H/ACA lobe, respectively. **d**, Close-up view of the density of DNA substrate-hTR template interactions (see also Fig. 2b). **e**, Close-up view of density of the DNA substrate and neighboring TERT residues (see also Extended Data Fig. 6d). **f**, Close-up view of density of the RNA template region and neighboring TERT residues (see also Extended Data Fig. 6e). **g**, Density of the P6.1 hairpin of the CR4/5 domain. Labelled residues are highlighted in Fig. 3a. **h**, Close-up review of the density of the P6.1 stem loop interacting with residues of the CTE domain of TERT (see also Fig. 3a and panel (**g**)). **i**, Close-up view of the density of residue L1019 of TERT, which interacts with the two flipped-out nucleotides, U177 of the PK and U307 of the P6.1 stem loop as highlighted in Fig. 3b. **j**, Representative density of the PK containing the base-triples, which are highlighted in black. Nucleotide U113 is modelled but not visible in this view. **k**, Density of the H- and ACA-boxes (see also Extended Data Fig. 3p for a related view). **l**, Density of the P8 stem loop (see also Extended Data Fig. 3o for a related view).

Europe PMC Funders Author Manuscripts

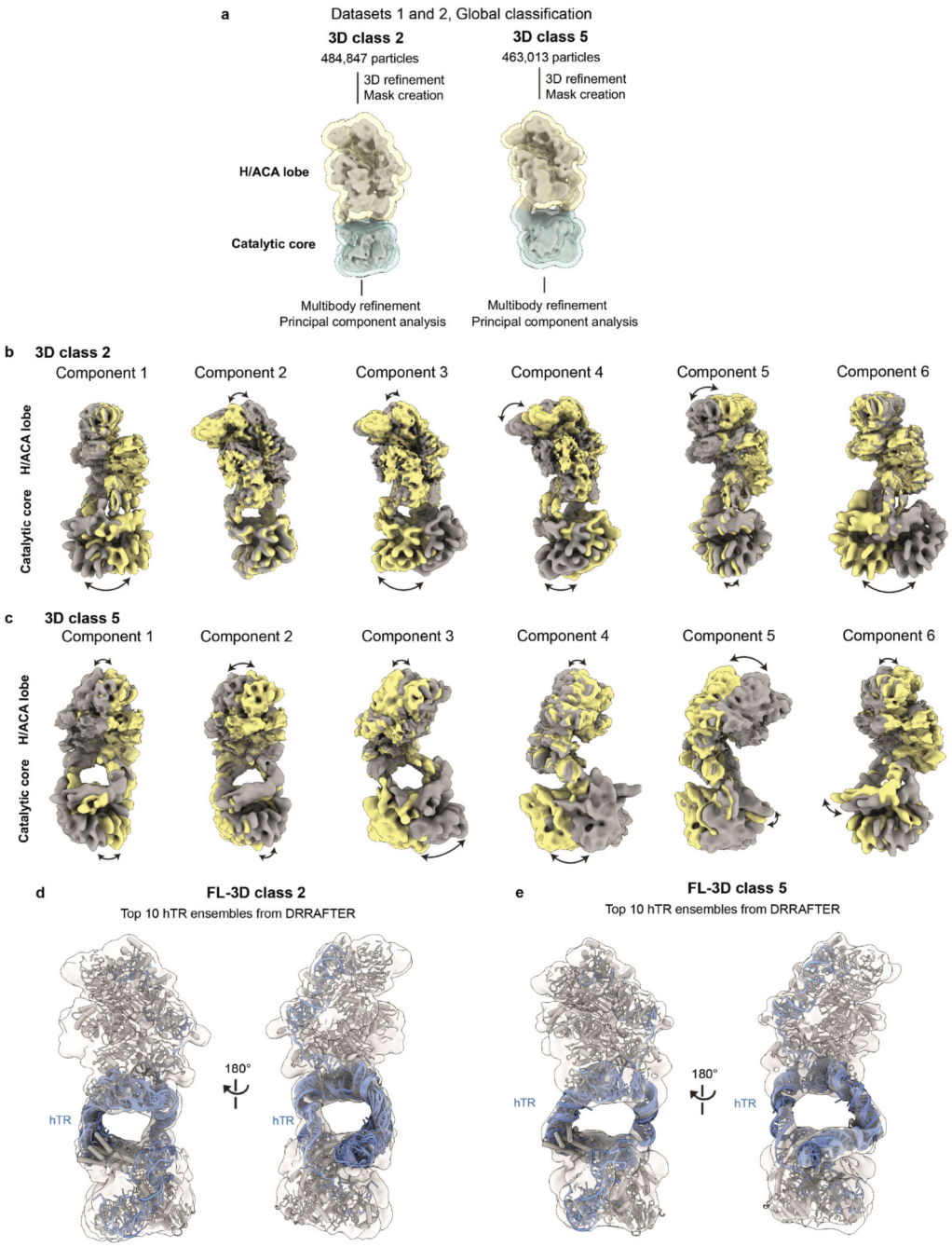

Extended Data Figure 5. Multibody refinement and conformational dynamics analysis of the full-length structure.

a, Summary of the multibody refinement strategy and principal component analysis[13]. The best two subsets from global 3D classification were subjected to multibody refinement using two masks for the H/ACA lobe (yellow) and the catalytic core (cyan). **b**, Principal component analysis for 3D class 2. **c**, Principal component analysis for 3D class 5. The first and last frames of the eigenvector series of the first 6 principal components are shown. Curved arrows indicate the movements. **d**, Top 10 hTR ensembles modelled by DRRAFTER

Europe PMC Funders Author Manuscripts

into the refined FL 3D class 2 map (see Supplementary Data 2). **e**, Top 10 hTR ensembles modelled by DRRAFTER into the refined FL 3D class 5 map (see Supplementary Data 3). hTR is shown in blue, and the protein subunits are in grey.

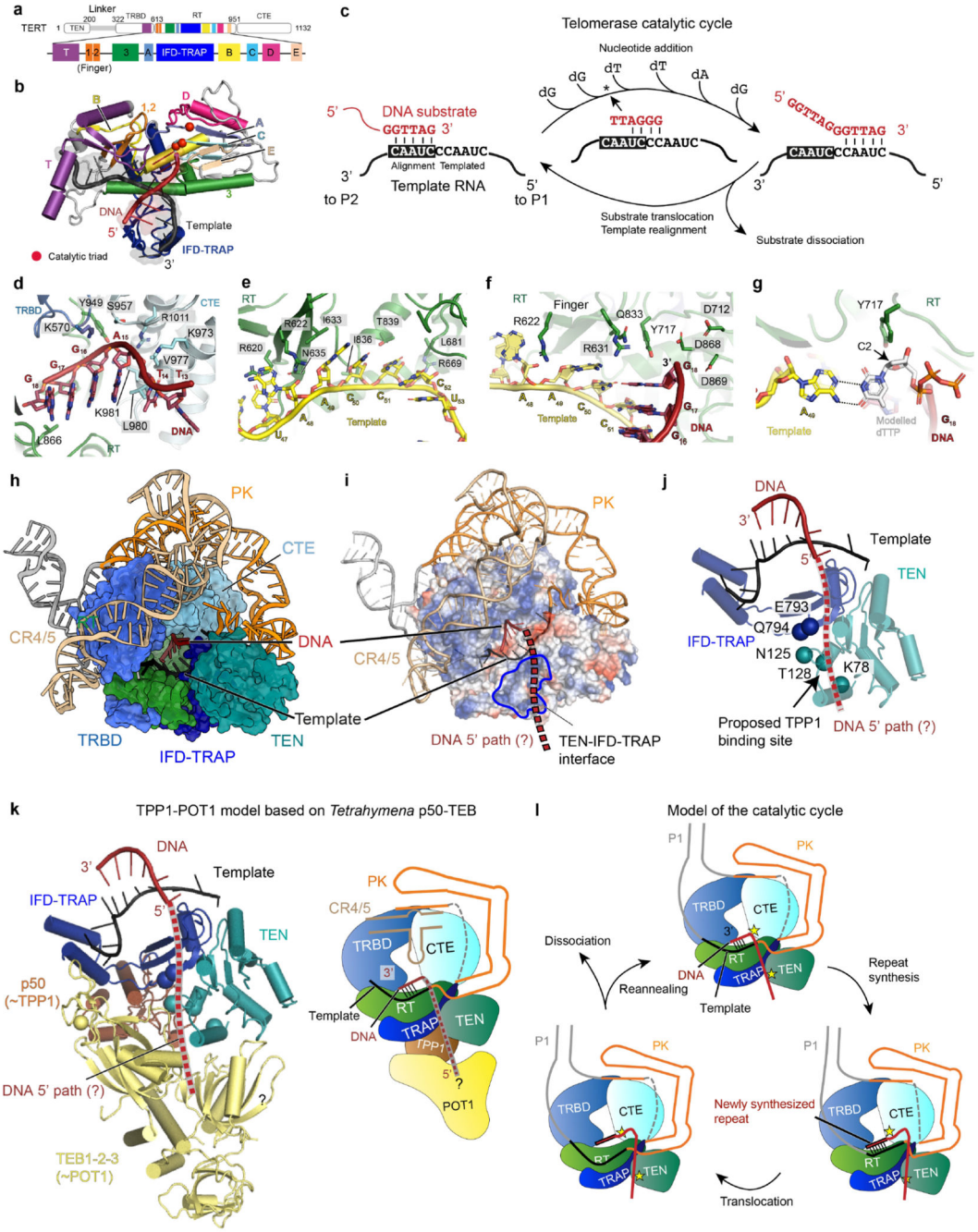

Extended Data Figure 6. Telomerase catalytic cycle and DNA path.

a, Domain architecture of human TERT and conserved motifs commonly observed in reverse transcriptases[70]. **b**, TERT conserved motifs shown in (**a**) and their interactions with the template and DNA substrate. **c**, A model for the telomerase catalytic cycle. The template

Europe PMC Funders Author Manuscripts

region of hTR is divided into an alignment region and a templated region. The telomeric DNA repeat first binds to the alignment region, followed by 6 consecutive nucleotide additions using the templated region. After the synthesis of the full telomeric repeat, the DNA substrate translocates to bind the alignment region to start another round of repeat synthesis. The state captured in our structure is indicated with an asterisk. **d**, Interactions between the 3' telomeric TTAGGG repeat of the substrate and TERT. **e**, Interactions between the template region of hTR and TERT. **f**, TERT active site in a pre-nucleotide state. D712, D868 and D869 form the catalytic triad for nucleotide addition. See also Extended Data Fig. 3b. **g**, Modelled dTTP (PDB 1T3N[22]) in the vacant nucleotide site of TERT. The C2 ribose is indicated. **h**, Structure of human TERT with PK/t and CR4/5 domains of hTR and DNA. **i**, Electrostatic surface potential of human TERT with hTR and the DNA substrate shown in the same view as (**h**). The highlighted human TEN-IFD-TRAP interface (in blue) is positively charged and could potentially bind the 5' end of the DNA substrate in human telomerase. **j**, IFD-TRAP and TEN domains of TERT with residues known to affect TPP1 binding to TERT highlighted as spheres[71]. The proposed DNA path would bring it close to the proposed TPP1 binding site on the TEN domain. **k**, Model of TPP1-POT1 bound to human TEN domain based on the *Tetrahymena* p50-TEB complex. Despite the similar overall domain arrangements, the domains of *Tetrahymena* and human TERT do not align well as whole. To obtain the model, we superposed the *Tetrahymena* TEN domain-p50-TEB1-2-3 complex (PDB 6D6V[16]) onto the human TEN domain. **l**, Model of telomerase catalytic cycle. Telomerase template RNA binds the telomeric DNA substrate by base-pairing. The DNA binding sites on TERT are indicated with the yellow stars. One binding site is provided by motif T and the CTE domain of TERT near the active site, as observed in the structure (Fig. 2d and panel (**d**)). The second binding site is proposed to be provided by the TEN domain at the 5' end of the DNA. After the synthesis of a full telomeric repeat, the nascent DNA undergoes translocation and rebinding to the template RNA. We propose that the two DNA binding sites form an anchor site to allow DNA retention for multiple rounds of repeat synthesis.

Europe PMC Funders Author Manuscripts

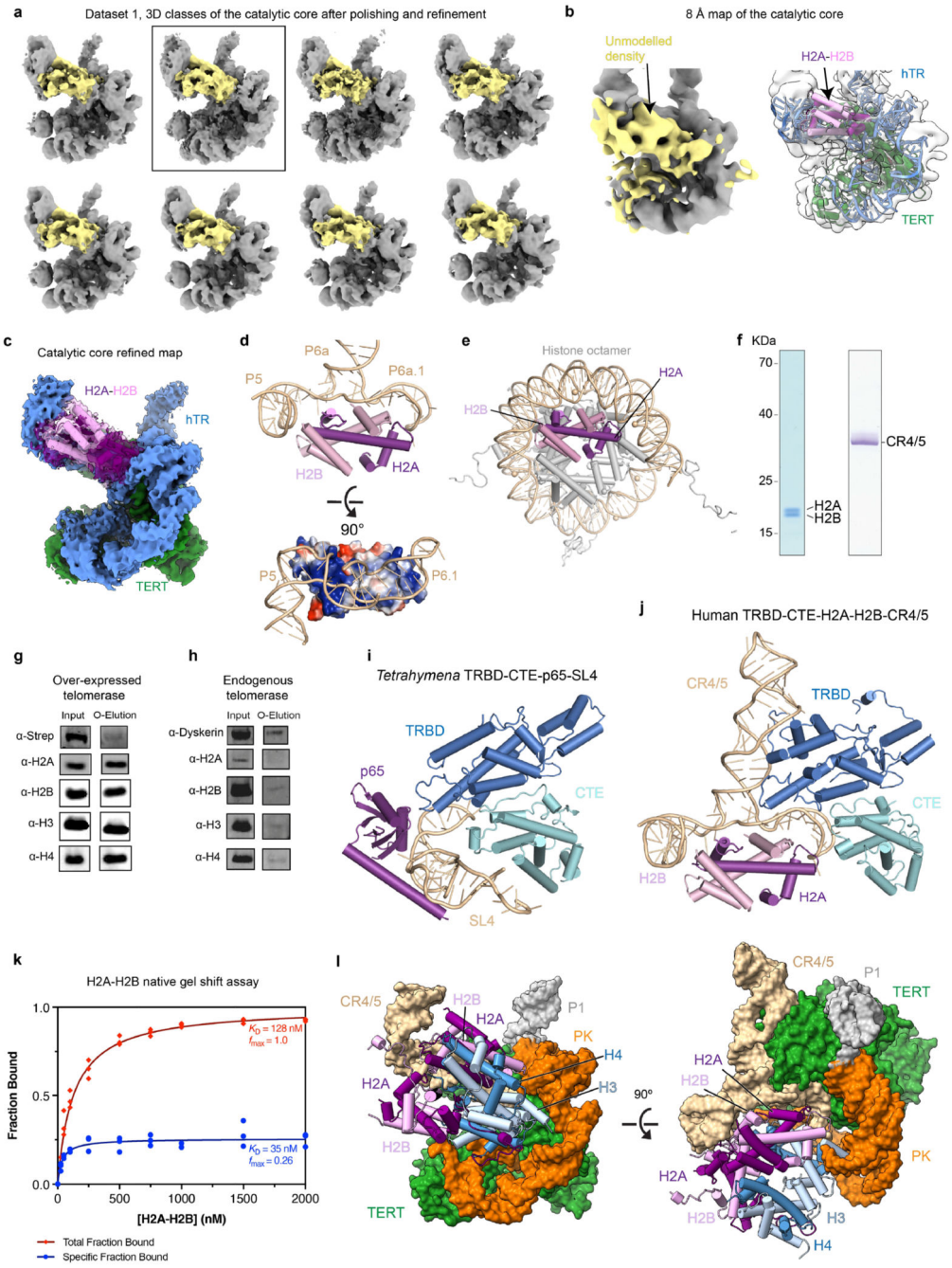

Extended Data Figure 7. Identification of H2A-H2B as human telomerase holoenzyme subunits.

a, 3D classification of the catalytic core (dataset 1) showing the presence of the unaccounted density (in yellow). The best class (boxed) has the most homogenous density and was selected for the final refinement. Similar observations were made with the second dataset. **b**, The 8 Å catalytic core map (in grey) with the previously unmodelled density (in yellow)[3] (left panel) and with the model of the catalytic core obtained from this work fitted into it (right panel). The density assigned as the histone H2A-H2B dimer coincided with the unmodelled density from the previous work. **c**, The refined catalytic core map with hTR,

Europe PMC Funders Author Manuscripts

TERT and H2A-H2B segmented in different colors. **d**, Interactions between CR4/5 and the H2A-H2B dimer in human telomerase. The bottom panel shows the electrostatic surface potential of the histone dimer and the positively charged surface used for interacting with the CR4/5. **e**, Nucleosome structure with the H2A-H2B dimer colored and oriented the same way as shown in **d**. This shows that the H2A-H2B uses the same surface to bind both nucleosomal DNA and CR4/5 (PDB ID 1KX5 (ref. 27)). **f**, Purified H2A-H2B and CR4/5 RNA used for EMSA in Fig. 3f. No RNA ladders were loaded with the CR4/5 RNA. **g**, Immunoblots of crude lysate of 293T cells transfected with Twin-Strep TERT and hTR expression constructs (input) and O-elution from 2'-O-Methyl purification (Fig. 3c). These samples were immunoblotted for Strep, H2A, H2B, H3 and H4. The presence of H2A, H2B, H3 and H4 is also confirmed by mass spectrometry (Supplementary Data 4). **h**, Immunoblots of crude lysate of 293T cells (input) and O-elution from 2'-O-Methyl purification. These samples were immunoblotted for dyskerin, H2A, H2B, H3 and H4. **i**, Structure of the *Tetrahymena* TRBD-CTE-p65 and stem loop 4 (SL4) (PDB 6D6V[16]). **j**, Structure of human TRBD-CTE-H2A-H2B and CR4/5. **k**, Quantification of the electrophoretic mobility shift assays shown in Fig. 3f for K_d determination. —Total Fraction Bound‖ reflects quantification of free probe depletion against total probe with increasing histone concentration. —Specific Fraction Bound‖ reflects quantification of increasing discrete shifted complex band against total probe with increasing histone concentration. Points represent values from three independent replicates (Supplementary Fig. 1). **h**, Superposition of the histone octamer structure, with flexible histone tails removed, onto the H2A-H2B dimer bound to the human telomerase catalytic core in two different views (PDB 1KX5 (ref. 27)).

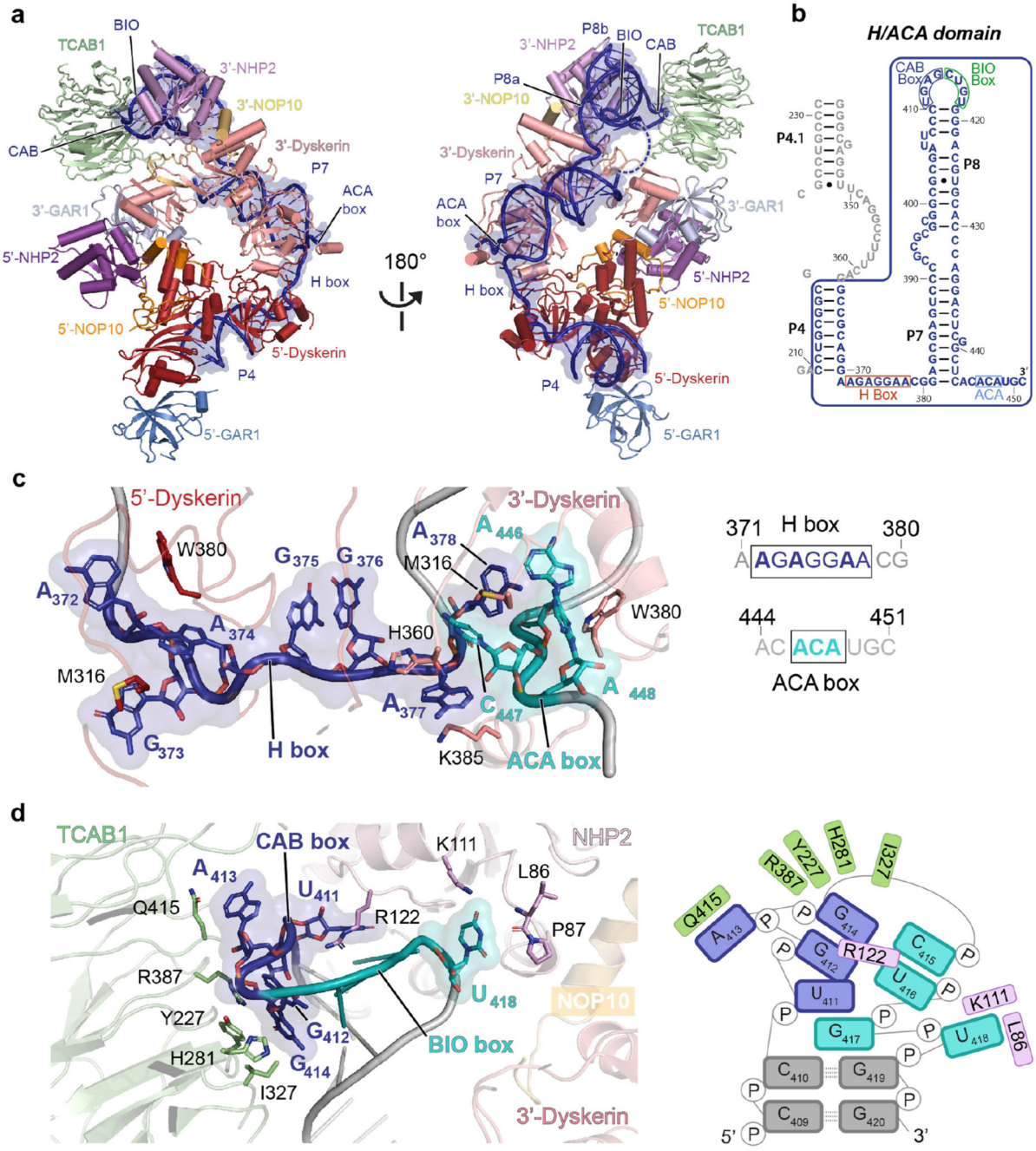

Extended Data Fig. 8. H/ACA RNP and molecular interactions of conserved RNA motifs.

a, Front (right) and back (left) views of the H/ACA RNP with subunits colored as indicated. **b**, Secondary structure schematic of the H/ACA domain of hTR. **c**, Close-up view (left panel) of the H- and ACA-boxes and their interactions with each other and with the two dyskerin molecules (see also Extended Data Figs. 3p, 4k). The right panel shows their sequences with conserved nucleotides highlighted in bold. **d**, Close-up view (left panel) of P8 stem loop and interactions between the CAB- and BIO-boxes with TCAB1 and NHP2

(see also Extended Data Figs. 3o, 4l). A schematic diagram of these interactions is shown in the right panel.

Extended Data Table 1

Cryo-EM data collection, refinement and validation statistics

	H/ACA lobe EMDB-12177 PDB 7BGB	**Catalytic core EMDB-12174 PDB 7BG9**	**FL-3D class 2 EMDB-12175**	**FL-3D class 5 EMDB-12176**
Data collection and processing				
Magnification				
Voltage (kV)	300	300	300	300
Electron exposure ($e^-/Å^2$)	47	47	47	47
Defocus range (μm)	1.2-3.2	1.2-3.2	1.2-3.2	1.2-3.2
Pixel size (Å)	1.11	1.11	1.11	1.11
Symmetry imposed	C1	C1	C1	C1
Initial particle images (no.)	15,760,434	15,760,434	15,760,434	15,760,434
Final particle images (no.)	204,665	168,538	484,847	463,013
Map resolution (Å)	3.40	3.81	4.53	6.63
FSC threshold	0.143	0.143	0.143	0.143
Map resolution range (Å)	3.3-7.0	3.7-7.0	3.9-16	4.5-15
Refinement				
Initial model used (PDB code)	Ab initio	Ab initio		
Model resolution (Å)	3.62	3.98		
FSC threshold	0.5	0.5		
Model resolution range (Å)	3.3-7.0	3.7-7.0		
Map sharpening *B* factor ($Å^2$)	-104	-80		
Model composition				
Non-hydrogen atoms	14538	14233		
Protein residues	1574	1085		
Nucleotides	92	262		
B factors ($Å^2$)				
Protein	232.27	206.07		
Nucleotide	255.78	267.64		
R.m.s. deviations				
Bond lengths (Å)	0.013	0.013		
Bond angles (°)	1.591	1.620		
Validation				
MolProbity score	2.37 (99^{th})	2.07 (100^{th})		
Clashscore	16.5 (97^{th})	8.09 (97^{th})		
Poor rotamers (%)	0.72	0.75		
Ramachandran plot				

	H/ACA lobe EMDB-12177 PDB 7BGB	Catalytic core EMDB-12174 PDB 7BG9	FL-3D class 2 EMDB-12175	FL-3D class 5 EMDB-12176
Favored (%)	85.56	86.46		
Allowed (%)	14.25	11.95		
Disallowed (%)	0.19	1.59		

Extended Data Table 2
Modelling of protein and RNA components

	Subunit	Total residues	M.W. (KDa)	Modelled	Chain name
Catalytic Core	TERT	1132	127	TEN: 11-60, 76-100, 125-179	A
				TRBD: 322-415, 444-613	
				RT: 614-720, 816-951	
				IFD-TRAP: 721-815	
				CTE: 952-1132	
	hTR	451	146	P1 and PK/Template: 26-149, 163-200	B
				CR4/5: 238-248, 251-333	
	H2A	130	14	18-99	L
	H2B	166	18	36-125	M
	DNA	18	6	13-18	N
H/ACA	5’-Dyskerin	514	57	36-185, 194-400	C
	5’-GAR1	217	21	70-158	D
	5’-NHP2	153	17	25-152	E
	5’-NOP10	64	8	1-62	F
	3’-Dyskerin	514	57	48-185, 192-392	G
	3’-GAR1	217	21	66-159	H
	3’-NHP2	153	17	25-152	I
	3’-NOP10	64	8	1-64	J
	hTR	451	146	362-392 211-218 397-449	B
	TCAB1	548	59	151-198, 210-317, 325-441, 453-485, 504-510	K

Supplementary Material

Refer to Web version on PubMed Central for supplementary material.

Acknowledgements

We thank the MRC-LMB EM facility staff for access and support of electron microscopy sample preparation and data collection; J. Grimmett and T. Darling for maintaining the computing facility; LMB mass spectrometry facility for running mass-spectrometry experiments; Steve Scotcher and the LMB workshop team for making our electrophoresis gel systems; K. Muir and D. Barford for sharing human histone expression constructs; Kalli Kappel

for advice on DRRAFTER modelling; Nagai, Löwe and Passmore labs for sharing reagents and equipment; the Collins and Nogales lab members for past technical support; and D. Barford, A. Carter, E. Nogales, L. Passmore and S. Scheres for critical reading of the manuscript. R.G. is supported by a National Science Foundation Graduate Fellowship. This work was funded by a UKRI-Medical Research Council grant to T. H. D. N. (MC_UP_1201/19), an N.I.H. grant to K.C. (GM054198), and N.I.H. grants to R.D. (GM122579 and GM121487).

Data availability

Raw gel source data are provided in Supplementary Fig. 1. Replicates of the activity assays and immunoblotting experiments shown in Fig. 3d and 3e and quantification are included in Supplementary Fig. 2. Full mass spectrometry data and coordinates of hTR from DRRAFTER modeling are provided in Supplementary Information. Cryo-EM maps of the catalytic core, H/ACA lobes and the whole telomerase maps (class 2 and class 5) with both lobes will be deposited with the Electron Microscopy Data Bank under accession number EMD-12174, EMD-12177, EMD-12175, and EMD-12176. Refined atomic coordinates for the catalytic core and H/ACA lobes will be deposited with the Protein Data Bank under accession number PDB-7BG9 and PDB-7BGB. The rigid-body fitted models of the catalytic core and the H/ACA lobes into the whole telomerase maps (class 2 and class 5) are included as a Pymol session in Supplementary Data 2, 3. The BALBES database was provided internally by the BALBES developers and is available upon request.

References

1. Levy MZ, Allsopp RC, Futcher AB, Greider CW, Harley CB. Telomere end-replication problem and cell aging. J Mol Biol. 1992; 225:951–960. [PubMed: 1613801]
2. Shay JW. Role of Telomeres and Telomerase in Aging and Cancer. Cancer Discov. 2016; 6:584–593. [PubMed: 27029895]
3. Nguyen THD, et al. Cryo-EM structure of substrate-bound human telomerase holoenzyme. Nature. 2018; 557:190–195. [PubMed: 29695869]
4. Blackburn EH, Collins K. Telomerase: an RNP enzyne synthesizes DNA. Cold Spring Harb Perspect Biol. 2011; 3 a003558 [PubMed: 20660025]
5. Lingner J, et al. Reverse transcriptase motifs in the catalytic subunit of telomerase. Science. 1997; 276:561–567. [PubMed: 9110970]
6. Wu RA, Upton HE, Vogan JM, Collins K. Telomerase Mechanism of Telomere Synthesis. Annu Rev Biochem. 2017; 86:439–460. [PubMed: 28141967]
7. MacNeil DE, Bensoussan HJ, Autexier C. Telomerase regulation from beginning to the end. Genes(Basel). 2016; 7:64.
8. Yu Y-T, Meier UT. RNA-guided isomerization of uridine to pseudouridine—pseudouridylation. RNA Biol. 2014; 11:1483–1494. [PubMed: 25590339]
9. Sarek G, Marzec P, Margalef P, Boulton SJ. Molecular basis of telomere dysfunction in human genetic diseases. Nat Struct Mol Biol. 2015; 22:867–874. [PubMed: 26581521]
10. Li L, Ye K. Crystal structure of an H/ACA box ribonucleoprotein particle. Nature. 2006; 443:302–307. [PubMed: 16943774]
11. Li S, et al. Reconstitution and structural analysis of the yeast box H/ACA RNA-guided pseudouridine synthase. Genes Dev. 2011; 25:2409–2421. [PubMed: 22085967]
12. Bai, X-c; Rajendra, E; Yang, G; Shi, Y; Scheres, SHW. Sampling the conformational space of the catalytic subunit of human γ-secretase. eLife. 2015; 4 e11182 [PubMed: 26623517]
13. Nakane T, Kimanius D, Lindahl E, Scheres SHW. Characterisation of molecular motions in cryo-EM single-particle data by multi-body refinement in RELION. eLife. 2018; 7 e36861 [PubMed: 29856314]
14. Kappel K, et al. De novo computational RNA modeling into cryo-EM maps of large ribonucleoprotein complexes. Nat Methods. 2018; 15:947–954. [PubMed: 30377372]

15. Podlevsky JD, Chen JJ. Evolutionary perspectives of telomerase RNA structure and function. RNA Biol. 2016; 13:720–732. [PubMed: 27359343]
16. Jiang J, et al. Structure of Telomerase with Telomeric DNA. Cell. 2018; 173:1179–1190. [PubMed: 29775593]
17. Wu RA, Tam J, Collins K. DNA-binding determinants and cellular thresholds for human telomerase repeat addition processivity. EMBO J. 2017; 36:1908–1927. [PubMed: 28495680]
18. Qi X, et al. RNA/DNA hybrid binding affinity determines telomerase template-translocation efficiency. EMBO J. 2012; 31:150–161. [PubMed: 21989387]
19. Bryan TM, Goodrich KJ, Cech TR. A mutant of Tetrahymena telomerase reverse transcriptase with increased processivity. J Biol Chem. 2000; 275:24199–24207. [PubMed: 10807925]
20. Schaich MA, et al. Mechanisms of nucleotide selection by telomerase. eLife. 2020; 9 e55438 [PubMed: 32501800]
21. Miller MC, Liu JK, Collins K. Template definition by Tetrahymena telomerase reverse transcriptase. EMBO J. 2000; 19:4412–4422. [PubMed: 10944124]
22. Nair DT, Johnson RE, Prakash S, Prakash L, Aggarwal AK. Replication by human DNA polymerase-I occurs by Hoogsteen base-pairing. Nature. 2004; 430:377–380. [PubMed: 15254543]
23. Chen JL, Opperman KK, Greider CW. A critical stem-loop structure in the CR4-CR5 domain of mammalian telomerase RNA. Nucleic Acids Res. 2002; 30:592–597. [PubMed: 11788723]
24. Robart AR, Collins K. Investigation of human telomerase holoenzyme assembly, activity, and processivity using disease-linked subunit variants. J Biol Chem. 2010; 285:4375–4386. [PubMed: 20022961]
25. Kim N, Theimer CA, Mitchell JR, Collins K, Feigon J. Effect of pseudouridylation on the structure and activity of the catalytically essential P6.1 hairpin in human telomerase RNA. Nucleic Acids Res. 2010; 38:6746–6756. [PubMed: 20554853]
26. Long F, Vagin AA, Young P, Murshudov GN. BALBES: a molecular-replacement pipeline. Acta Crystallogr D Biol Crystallogr. 2008; 64:125–132. [PubMed: 18094476]
27. Davey CA, Sargent DF, Luger K, Maeder AW, Richmond TJ. Solvent Mediated Interactions in the Structure of the Nucleosome Core Particle at 1.9Å Resolution. J of Mol Biol. 2002; 319:1097–1113. [PubMed: 12079350]
28. Schnapp G, Rodi H-P, Rettig WJ, Schnapp A, Damm K. One-step affinity purification protocol for human telomerase. Nucleic Acids Res. 1998; 26:3311–3313. [PubMed: 9628936]
29. Palka C, Forino N, Hentschel J, Das R, Stone MD. Folding heterogeneity in the essential human telomerase RNA three-way junction. RNA. 2020; 26:1787–1800. [PubMed: 32817241]
30. Fu D, Collins K. Distinct biogenesis pathways for human telomerase RNA and H/ACA small nucleolar RNAs. Mol Cell. 2003; 11:1361–1372. [PubMed: 12769858]
31. Egan ED, Collins K. An enhanced H/ACA RNP assembly mechanism for human telomerase RNA. Mol Cell Biol. 2012; 32:2428–2439. [PubMed: 22527283]
32. Tycowski KT, Shu MD, Kukoyi A, Steitz JA. A conserved WD40 protein binds the Cajal body localization signal of scaRNP particles. Mol Cell. 2009; 34:47–57. [PubMed: 19285445]
33. Venteicher AS, et al. A human telomerase holoenzyme protein required for Cajal body localization and telomere synthesis. Science. 2009; 323:644–648. [PubMed: 19179534]
34. Theimer CA, et al. Structural and functional characterization of human telomerase RNA processing and cajal body localization signals. Mol Cell. 2007; 27:869–881. [PubMed: 17889661]
35. Jády BE, Bertrand E, Kiss T. Human telomerase RNA and box H/ACA scaRNAs share a common Cajal body-specific localization signal. J Cell Biol. 2004; 164:647–652. [PubMed: 14981093]
36. Parks JW, Stone MD. Coordinated DNA dynamics during the human telomerase catalytic cycle. Nat Commun. 2014; 5:4146. [PubMed: 24923681]
37. Patrick EM, Slivka JD, Payne B, Comstock MJ, Schmidt JC. Observation of processive telomerase catalysis using high-resolution optical tweezers. Nat Chem Biol. 2020; 16:801–809. [PubMed: 32066968]
38. Nandakumar J, et al. The TEL patch of telomere protein TPP1 mediates telomerase recruitment and processivity. Nature. 2012; 492:285–289. [PubMed: 23103865]

39. Latrick CM, Cech TR. POT1-TPP1 enhances telomerase processivity by slowing primer dissociation and aiding translocation. EMBO J. 2010; 29:924–933. [PubMed: 20094033]
40. Zhong FL, et al. TPP1 OB-fold domain controls telomere maintenance by recruiting telomerase to chromosome ends. Cell. 2012; 150:481–494. [PubMed: 22863003]
41. Sexton AN, Youmans DT, Collins K. Specificity requirements for human telomere protein interaction with telomerase holoenzyme. J Biol Chem. 2012; 287:34455–34464. [PubMed: 22893708]
42. Upton HE, Hong K, Collins K. Direct single-stranded DNA binding by Teb1 mediates the recruitment of Tetrahymena thermophila telomerase to telomeres. Mol Cell Biol. 2014; 34:4200–4212. [PubMed: 25225329]
43. Jiang J, et al. Structure of Tetrahymena telomerase reveals previously unknown subunits, functions, and interactions. Science. 2015; 350 aab4070 [PubMed: 26472759]
44. Witkin KL, Collins K. Holoenzyme proteins required for the physiological assembly and activity of telomerase. Genes Dev. 2004; 18:1107–1118. [PubMed: 15131081]
45. Stone MS, et al. Stepwise protein-mediated RNA folding directs assembly of telomerase ribonucleoprotein. Nature. 2007; 446:458–461. [PubMed: 17322903]
46. Greider CW. Regulating telomere length from the inside out: the replication fork model. Genes Dev. 2016; 30:1483–1491. [PubMed: 27401551]
47. Margalef P, et al. Stabilization of Reversed Replication Forks by Telomerase Drives Telomere Catastrophe. Cell. 2018; 172:439–453. [PubMed: 29290468]
48. Sauer PV, et al. Mechanistic insights into histone deposition and nucleosome assembly by the chromatin assembly factor-1. Nucleic Acids Res. 2018; 46:9907–9917. [PubMed: 30239791]
49. Wu RA, Dagdas YS, Yilmaz ST, Yildiz A, Collins K. Single-molecule imaging of telomerase reverse transcriptase in human telomerase holoenzyme and minimal RNP complexes. eLife. 2015; 4 e08363
50. Luger K, Rechsteiner TJ, Richmond TJ. Methods Enzymol. 1999; 304:3–19. [PubMed: 10372352]
51. Nguyen, THD. Structural and biochemical studies of spliceosomal activation. PhD thesis, University of Cambridge; 2014.
52. Goodrich, JA, Kugel, JF. Binding and Kinetics for Molecular Biologists. Cold Spring Harbor Laboratory Press; 2007.
53. Mastronarde DN. Automated electron microscope tomography using robust prediction of specimen movements. J Struct Biol. 2005; 152:36–51. [PubMed: 16182563]
54. Zivanov J, et al. New tools for automated high-resolution cryo-EM structure determination in RELION-3. eLife. 2018; 7 e42166 [PubMed: 30412051]
55. Rohou A, Grigorieff N. CTFFIND4: Fast and accurate defocus estimation from electron micrographs. J Struct Biol. 2015; 192:216–221. [PubMed: 26278980]
56. Zivanov J, Nakane T, Scheres SHW. Estimation of high-order aberrations and anisotropic magnification from cryo-EM data sets in RELION-3.1. IUCrJ. 2020; 7:253–267.
57. Rosenthal PB, Henderson R. Optimal determination of particle orientation, absolute hand, and contrast loss in single-particle electron cryomicroscopy. J Mol Biol. 2003; 333:721–745. [PubMed: 14568533]
58. Chen S, et al. High-resolution noise substitution to measure overfitting and validate resolution in 3D structure determination by single particle electron cryomicroscopy. Ultramicroscopy. 2013; 135:24–35. [PubMed: 23872039]
59. Brown A, et al. Tools for macromolecular model building and refinement into electron cryo-microscopy reconstructions. Acta Crystallogr D Biol Crystallogr. 2015; 71:136–153. [PubMed: 25615868]
60. Vagin A, Teplyakov A. Molecular replacement with MOLREP. Acta Crystallogr D. 2010; 66:22–25. [PubMed: 20057045]
61. Casañal A, Lohkamp B, Emsley P. Current developments in Coot for macromolecular model building of Electron Cryo-microscopy and Crystallographic Data. Protein Sci. 2020; 29:1055–1064.

62. Chou F-C, Echols N, Terwilliger TC, Das R. RNA Structure Refinement Using the ERRASER-Phenix Pipeline. Methods Mol Biol. 2016; 1320:269–282. [PubMed: 26227049]

63. Afonine PV, et al. Towards automated crystallographic structure refinement with phenix.refine. Acta Crystallogr D. 2012; 68:352–367. [PubMed: 22505256]

64. Murshudov GN, et al. REFMAC5 for the refinement of macromolecular crystal structures. Acta Crystallogr D. 2011; 67:355–367. [PubMed: 21460454]

65. Nicholls RA, Fischer M, McNicholas S, Murshudov GN. Conformation-independent structural comparison of macromolecules with ProSMART. Acta Crystallogr D. 2014; 70:2487–2499. [PubMed: 25195761]

66. Williams CJ, et al. MolProbity: More and better reference data for improved all-atom structure validation. Protein Sci. 2018; 27:293–315. [PubMed: 29067766]

67. Tang G, et al. EMAN2: an extensible image processing suite for electron microscopy. J Struct Biol. 2007; 157:38–46. [PubMed: 16859925]

68. Goddard TD, et al. UCSF ChimeraX: Meeting modern challenges in visualization and analysis. Protein Sci. 2018; 27:14–25. [PubMed: 28710774]

69. Pettersen EF, et al. UCSF Chimera--a visualization system for exploratory research and analysis. J Comput Chem. 2004; 25:1605–1612. [PubMed: 15264254]

70. Podlevsky JD, Bley CJ, Omana RV, Qi X, Chen JJ. The telomerase database. Nucleic Acids Res. 2008; 36 D339-343 [PubMed: 18073191]

71. Tesmer VM, Smith EM, Danciu O, Padmanaban S, Nandakumar J. Combining conservation and species-specific differences to determine how human telomerase binds telomeres. Proc Natl Acad Sci. 2019; 116:26505–26515.

Europe PMC Funders Author Manuscripts

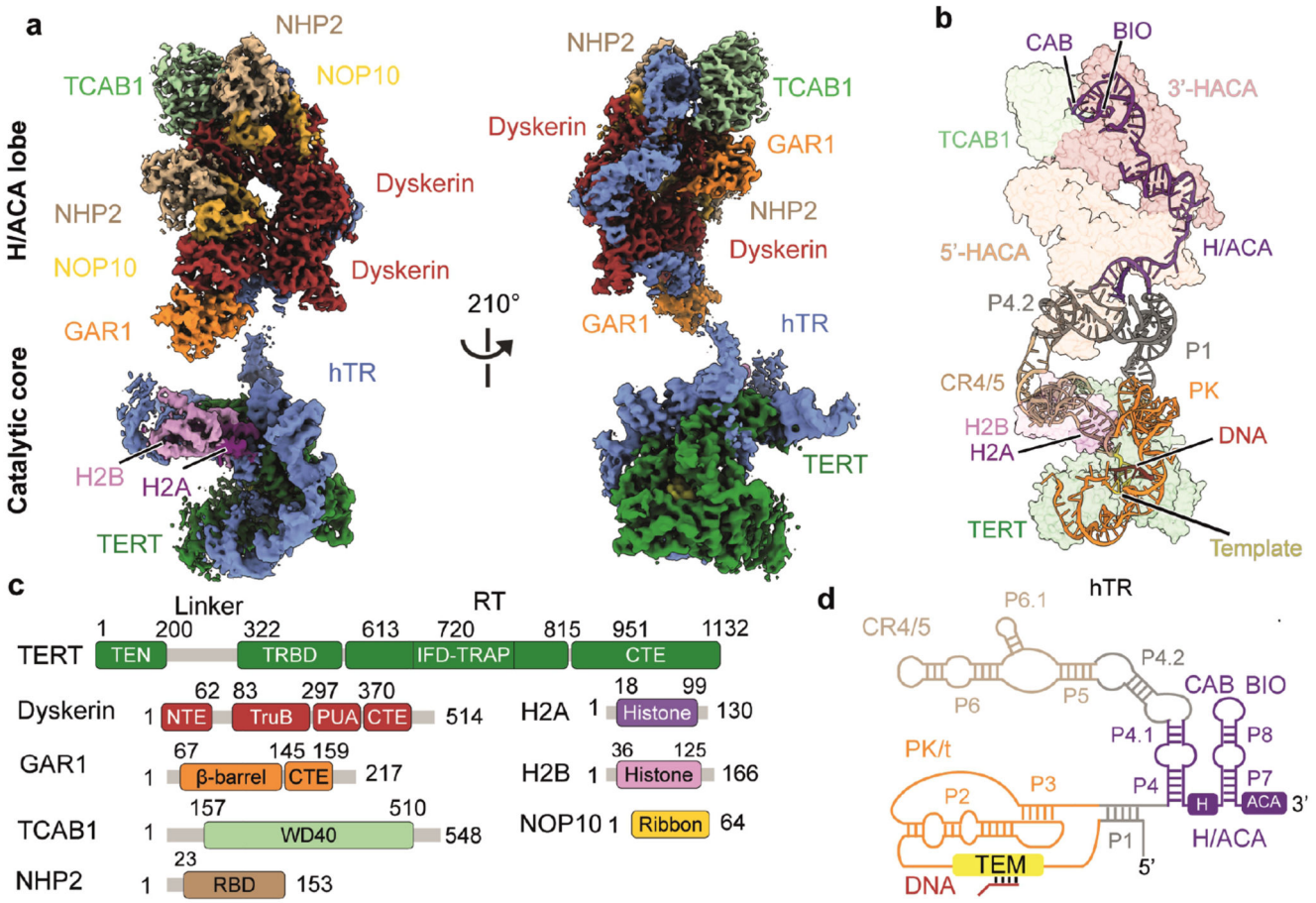

Figure 1. Cryo-EM structure of human telomerase holoenzyme.

a, Front (left) and back (right) views of the composite cryo-EM maps of the catalytic core and the H/ACA lobe at 3.8 Å and 3.4 Å, respectively, with subunits colored as indicated. **b**, Front view of the structure with hTR and the DNA substrate highlighted. **c**, Domain architectures of protein subunits. TEN, telomerase essential N-terminal domain; TRBD, telomerase RNA-binding domain; RT, reverse transcriptase; IFD-TRAP, insertion in fingers-TRAP domain; CTE, C-terminal extension; NTE, N-terminal extension; TruB, tRNA pseudouridine synthase B-like domain; PUA, pseudouridine synthase and archaeosine transglycosylase; WD40, Trp-Asp 40 repeat domain; RBD, RNA-binding domain. **d**, Secondary structure of hTR and DNA substrate (see also Extended Data Fig. 4a). TEM, template; PK/t, pseudoknot/template; CR4/5, conserved regions 4 and 5; BIO, biogenesis-promoting.

Europe PMC Funders Author Manuscripts

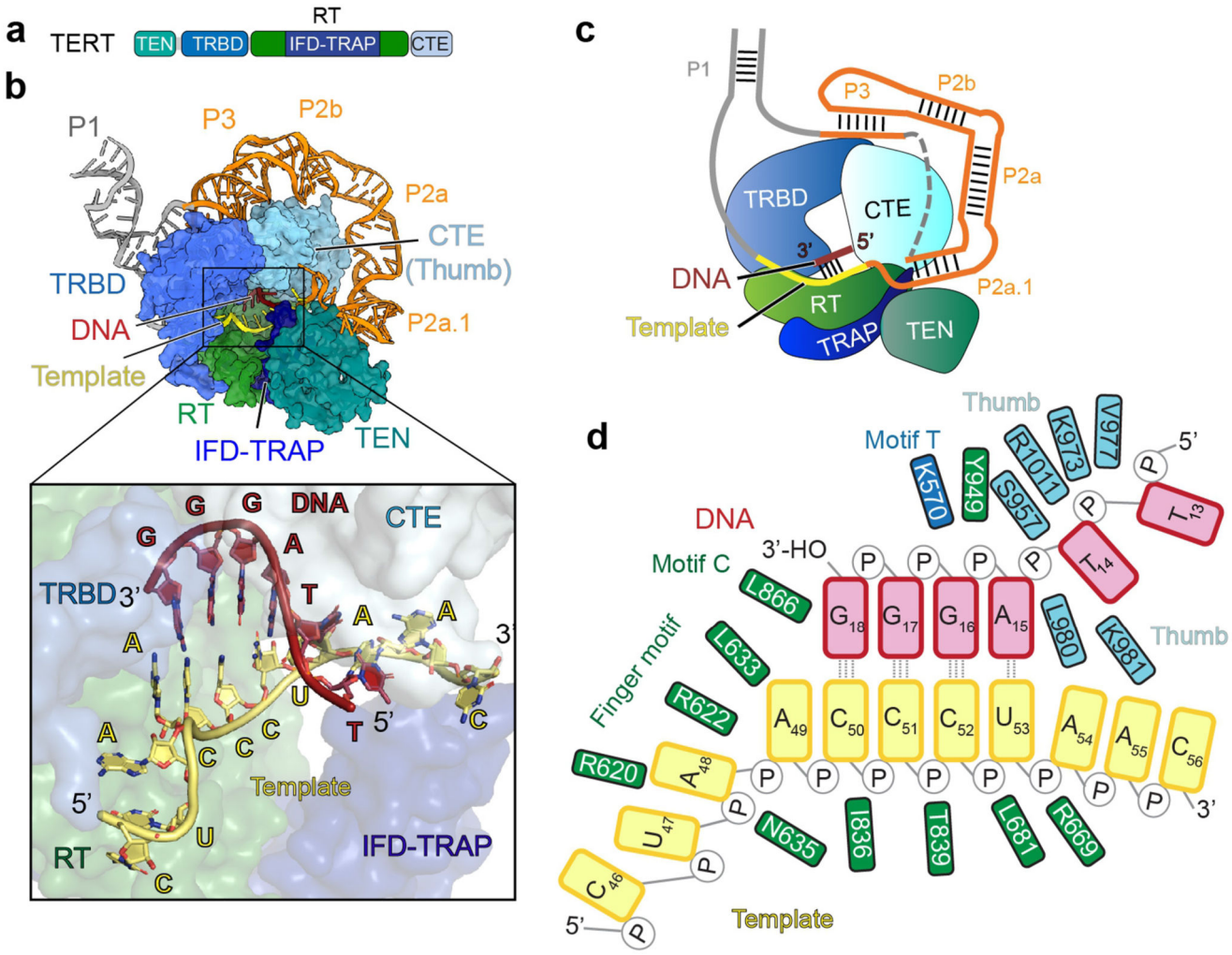

Figure 2. Human telomerase catalytic core.

a, Domain architecture of TERT. This domain color scheme is used throughout the paper unless otherwise stated. **b,** TERT structure with the PK/t domain of hTR and DNA substrate. The inset shows a close-up view of the DNA substrate-RNA template duplex in TERT active site (see also Extended Data Fig. 4d) **c**, Cartoon of TERT domains, hTR PK/t domain and the DNA substrate. **d**, Schematic diagram of the DNA-RNA duplex observed in our structure and interactions with TERT residues (see also Extended Data Figs. 6d-f).

Europe PMC Funders Author Manuscripts

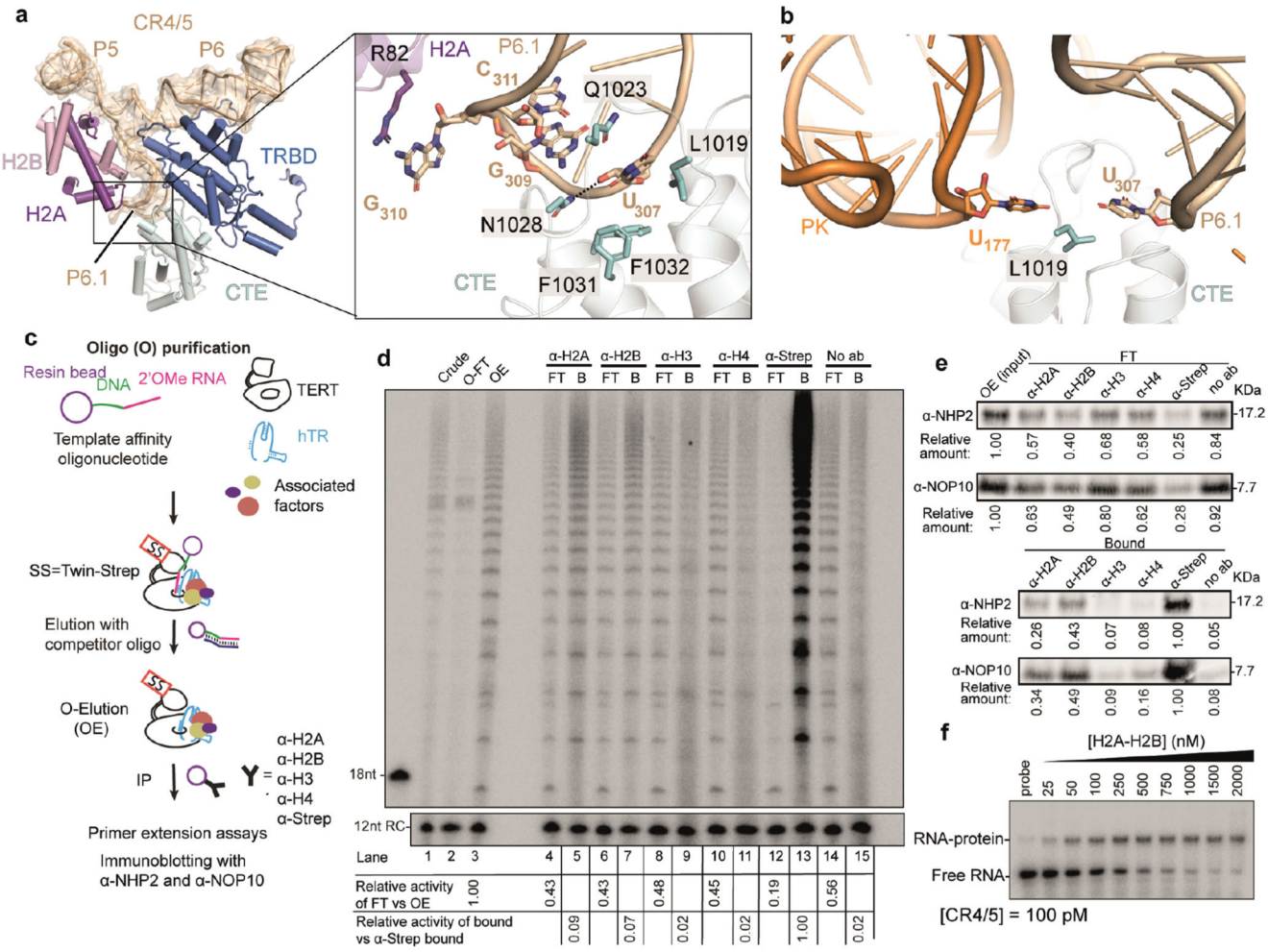

Figure 3. CR4/5 interactions with TERT and novel H2A-H2B subunits.

a, CR4/5 domain of hTR and its interaction with TERT TRBD and CTE domains and the histone H2A-H2B dimer. The inset provides a close-up view to highlight the recognition of the P6.1 apical loop by TERT and H2A (see also Extended Data Figs. 4g, h). **b**, The close proximity between the PK (orange) and P6.1 stem loop (wheat) (see also Extended Data Fig. 4i). **c**, Schematic of 2'-O-Methyl oligo-purification coupled with immunoprecipitation (IP) to confirm the presence of H2A-H2B in human telomerase structure. SS, twin strep tag. **d**, Activity assay results of the IP shown in panel (**c**). Crude, input lysate; O-FT, flow-through from oligo-purification; OE, elution from oligo-purification; FT, flow-through from immunoprecipitation with each set of antibodies; B, bound sample on beads from immunoprecipitation with each set of antibodies; 12nt RC, 12-nucleotide recovery control; 18nt, 18-nucleotide marker. We performed two separate quantifications. Each FT activity was quantified relative to input (OE) activity. Each bound activity was quantified relative to anti-Strep IP positive control. All quantifications were normalised to the signal of the recovery control. **e**, Immunoblot analyses of the IP shown in panel (**c**). Each fraction was immunoblotted with NHP2 antibody (α-NHP2) and NOP10 antibody (α-NOP10). Signal from each flow though fraction (FT) was quantified relative to the input (OE) signal. Signal

from each bound fraction (Bound) was quantified relative to the anti-Strep IP signal. **f**, Native electrophoretic mobility shift assays showing titration of purified H2A-H2B against ^{32}P end-labelled CR4/5 RNA. See Extended Data Fig. 7k for quantification. Experiments shown in **(d)-(f)** were done in three technical replicates (see also Supplementary Figs 1 and 2).

Europe PMC Funders Author Manuscripts

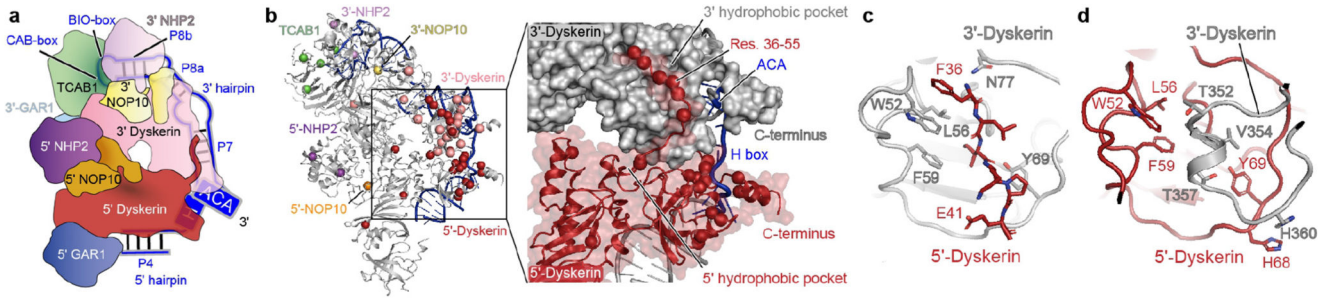

Figure 4. H/ACA RNP structure and human disease mutations.

a, Schematic of the H/ACA RNP showing hTR interactions with the H/ACA proteins. **b**, Overall structure of the H/ACA RNP with DC and HH disease mutations highlighted in spheres[9]. Close-up view of the disease mutation hotspot, which lies at the interface between the two dyskerin molecules (inset). **c**, The hydrophobic pocket of 3' dyskerin, which accommodates the N-terminal extension of the 5' dyskerin (see also Extended Data Fig. 3m). **d**, The hydrophobic pocket of 5' dyskerin, which accommodates helix 352-357 of 3' dyskerin (see also Extended Data Fig. 3n).

Europe PMC Funders Author Manuscripts